J Nanopart Res (2016) 18:195
DOI 10.1007/s11051-016-3502-2

RESEARCH PAPER

Synthesis of ZnO@γ-Fe_2O_3 core–shell nanocomposites by a facile thermal decomposition approach and their application in photocatalytic degradation of congo red

Sudheer Kumar Yadav · P. Jeevanandam

Received: 26 December 2015 / Accepted: 5 July 2016 / Published online: 15 July 2016

Abstract ZnO@γ-Fe_2O_3 core–shell nanocomposites were synthesized by a facile thermal decomposition approach. ZnO nanorods were first synthesized by calcination of zinc acetate at 300 °C, in air. γ-Fe_2O_3 nanoparticles were then deposited on the surface of ZnO nanorods by the thermal decomposition of iron acetylacetonate at 200 °C in diphenyl ether. The structure, composition, optical and magnetic properties of the nanocomposites were studied using an array of techniques. XRD results suggest the presence of γ-Fe_2O_3 nanoparticles and ZnO, and FE-SEM images indicate formation of shell of iron oxide on the ZnO nanorods. Transmission electron microscopy studies clearly show that ZnO possesses rod morphology (length = 1.1 ± 0.1 μm, diameter = 40.1 ± 7 nm) and TEM images of the ZnO@γ-Fe_2O_3 nanocomposites show uniform shell of γ-Fe_2O_3 coated on the ZnO nanorods and thickness of the γ-Fe_2O_3 shell varies from 10 to 20 nm. Diffuse reflectance spectra of ZnO@γ-Fe_2O_3 nanocomposites reveal extended optical absorption in the visible range (400–600 nm) and photoluminescence spectra indicate that the ZnO@γ-Fe_2O_3 nanocomposites exhibit enhanced defect emission. The ZnO@γ-Fe_2O_3 core–shell nanocomposites show superparamagnetic behaviour at room temperature. The core–shell nanocomposites exhibit enhanced visible-light driven photocatalytic degradation of congo red in an aqueous solution as compared to pure ZnO nanorods and γ-Fe_2O_3 nanoparticles. The enhanced photocatalytic activity is attributed to good visible-light absorption and effective charge separation at the interface of ZnO@γ-Fe_2O_3 core–shell nanocomposites.

Keywords ZnO@γ-Fe_2O_3 core–shell nanocomposites · Thermal decomposition · Photocatalytic degradation

Introduction

Nowadays, research efforts are being focused on the use of semiconductors as photocatalysts for the degradation of toxic organic compounds discharged from various industries (Chen et al. 2010a). Among various metal oxide semiconductor photocatalysts used for this purpose, ZnO has been of tremendous interest due to its high photosensitivity and wide band gap (3.3 eV). ZnO possesses many advantages that include low cost, high quantum efficiency and high photocatalytic activity. There are two drawbacks associated with ZnO as the photocatalyst, namely, high charge recombination rate and low efficiency

Electronic supplementary material The online version of this article (doi:10.1007/s11051-016-3502-2) contains supplementary material, which is available to authorized users.

S. K. Yadav · P. Jeevanandam (✉)
Department of Chemistry, Indian Institute of Technology Roorkee, Roorkee 247667, India
e-mail: jeevafcy@iitr.ac.in

when utilized under solar light (Kumar and Rao 2015). Various methods have been developed to reduce the recombination rate of photogenerated electrons and holes in ZnO and thus increase the utilization of visible light. Hybrid semiconductor nanostructures have been shown to be promising for the removal of toxic organic pollutants from waste water (Wang et al. 2013). The combination of semiconductors with small band gap with wide band gap semiconductors increases absorption of radiation in the visible range. γ-Fe_2O_3, a narrow band gap (1.9–2.2 eV) n-type semiconductor with absorption in the visible region, is a potential candidate that can act as a sensitizer under sunlight irradiation. The enhanced photocatalytic efficiency has been explained by a fast transfer of photogenerated electrons and holes from γ-Fe_2O_3 to ZnO (Liu et al. 2012).

ZnO–Fe_2O_3 nanocomposites have been intensively investigated for a wide variety of applications such as waste water treatment, water splitting, sensors, magnetic materials, lithium ion batteries and solar cells (Guskos et al. 2010; Hsu et al. 2015; Liu et al. 2012; Qin et al. 2012; Reda 2010; Zhang et al. 2011). ZnO–Fe_2O_3 nanocomposites have been prepared by different reported methods. Liu et al. have synthesized ZnO–Fe_2O_3 core–shell nanocomposites using microwave irradiation followed by thermal decomposition (Liu et al. 2012). Hsu et al. have synthesized ZnO@Fe_2O_3 core–shell nanocomposites by a two-step (hydrothermal and wet chemical) method (Hsu et al. 2015). Guskos et al. have synthesized ZnO–Fe_2O_3 nanocomposites by a wet chemical method (Guskos et al. 2010). Reda, Maya-Trevino et al. and Hernandez et al. have synthesized ZnO–Fe_2O_3 nanocomposites by sol–gel method (Hernández et al. 2007; Maya-Treviño et al. 2014; Reda 2010). Yin et al. have synthesized α-Fe_2O_3 decorated ZnO nanorods by impregnation deposition method (Yin et al. 2014). Abdullah Mirzaie et al. have synthesized ZnO–Fe_2O_3 nanocomposites by solid state reaction (Abdullah Mirzaie et al. 2012). Liu et al. have synthesized ZnO–Fe_2O_3 nanotube composites by photochemical deposition under UV light (Liu et al. 2015a, b). Fu et al. have synthesized ZnO–γ-Fe_2O_3 nanocomposites by solution route (Fu et al. 2008). Si et al. have prepared ZnO–Fe_2O_3 core–shell nanorods by solution phase hydrolysis method (Si et al. 2006). Balti et al. have synthesized Fe_2O_3 decorated ZnO nanorods by polyol method (Balti et al. 2014). Zhou et al. have synthesized ZnO–Fe_2O_3 core–shell heterostructures by hydrothermal method (Zhou et al. 2015). Chu et al. have synthesized ZnO microrods coated with iron oxide nanoparticles by low temperature hydrothermal method (Chu et al. 2008). Wu et al. have synthesized ZnO-γ-Fe_2O_3 hybrid nanomaterials by layer-by layer assembly technique (Wu et al. 2010). Mo et al. have synthesized ZnO-FeO_x core–shell nanorods by thermal decomposition of $Fe(acac)_3$ at 265 °C under nitrogen atmosphere (Mo et al. 2009). Most of the methods, reported so far, are complex, involve multi-steps, require surface modification of ZnO nanorods by polyelectrolytes (e.g. PAH/PSS/PAH, PAH = poly(allylamine hydrochloride), and PSS = poly(sodium 4-styrenesulphonate)) with reaction time of 30 min to 4 h and also require often special conditions such as an inert atmosphere.

In the present study, ZnO@γ-Fe_2O_3 core–shell nanocomposites have been prepared by a novel thermal decomposition method. ZnO nanorods with length 1.1 ± 0.1 μm and diameter 40.1 ± 7 nm were prepared by heating zinc acetate dihydrate at 300 °C, in air. Uniform layer of γ-Fe_2O_3 was then deposited by the thermal decomposition of $Fe(acac)_3$ in diphenyl ether at 200 °C in the presence of ZnO nanorods. After thorough characterization, the nanocomposites were explored as catalyst for photocatalytic degradation of congo red in an aqueous solution.

Experimental details

Chemicals and materials

The chemicals used were zinc acetate dihydrate (Rankem), iron acetylacetonate ($Fe(acac)_3$) (ACROS), diphenyl ether (Aldrich), congo red (SRL), ammonium oxalate (Sarabhai Chemicals), benzoquinone (Alfa Aesar), tertiary butyl alcohol (Rankem), methanol (Rankem), and Millipore® water. All the chemicals were used as received.

Synthesis

The ZnO@γ-Fe_2O_3 nanocomposites were prepared via a thermal decomposition method.

Synthesis of ZnO nanorods

The first step was the preparation of ZnO nanorods by solid-state thermal decomposition of zinc acetate dihydrate (Chandraiahgari et al. 2015). 2.0 g of zinc acetate dihydrate was crushed with the help of a mortar and pestle and was heated in a muffle furnace at 300 °C for 3 h at a heating rate of 2 °C/min, in air.

Synthesis of ZnO@γ-Fe_2O_3 core–shell nanocomposites

The ZnO@γ-Fe_2O_3 core–shell nanocomposites were synthesized by the thermal decomposition of $Fe(acac)_3$ in diphenyl ether at 200 °C in the presence of ZnO nanorods. Four different core–shell nanocomposites (ZF1, ZF2, ZF3 and ZF4) were prepared by varying the concentration of $Fe(acac)_3$ (Table 1). The reagents were added to 10 mL of diphenyl ether (boiling point = 257 °C) in a round bottom flask and refluxed in air at about 200 °C for 35 min. The precipitates obtained were centrifuged, washed with methanol and dried overnight under vacuum to obtain the ZnO@γ-Fe_2O_3 core–shell nanocomposites. For comparison, pure γ-Fe_2O_3 nanoparticles were also synthesized using the same method.

Photocatalytic activity

The photocatalytic experiments using ZnO@γ-Fe_2O_3 core–shell nanocomposites (ZF1, ZF2, ZF3 and ZF4) as the catalysts for the photodegradation of congo red in aqueous solutions were conducted as follows: 50 mg powder of each catalyst was suspended in 50 mL of congo red aqueous solution (50 mg L^{-1}) and the contents were stirred in dark for 60 min to reach adsorption–desorption equilibrium. Afterwards, the suspension was exposed to sunlight for various time intervals (0–90 min). The photocatalytic experiments under sunlight were carried out at Indian Institute of Technology Roorkee, Roorkee, India in the month of April 2015 between 12.00 noon and 2.00 pm. The intensity of solar radiation in Roorkee in the month of April was 280 W/m^2 (Ramachandra et al. 2011). At regular time intervals, 3 mL of the suspension was taken and centrifuged at 3500 rpm for 5 min to completely remove the catalyst. The concentration of congo red in the supernatant solution was analysed with the help of UV–Visible spectroscopy (Shimadzu UV-2450) by measuring the absorbance at 495 nm. The photocatalytic activity of pure ZnO nanorods and γ-Fe_2O_3 nanoparticles towards the photodegradation of congo red was also studied for comparison with that of the ZnO@γ-Fe_2O_3 core–shell nanocomposites. To verify the role of different oxidation species (h^+, $OH^{\cdot}$ and $O_2^{\cdot-}$) in the photocatalytic degradation of congo red, scavenger tests were carried out using different scavengers. The scavengers used were ammonium oxalate (h^+), benzoquinone ($O_2^{\cdot-}$), and tertiary butyl alcohol ($OH^{\cdot}$).

Table 1 Designation of various ZnO@γ-Fe_2O_3 nanocomposites prepared using different molar ratios of $Fe(acac)_3$ and ZnO

Sample code	ZnO (mmol)	$Fe(acac)_3$ (mmol)
γ-Fe_2O_3	–	1
ZF1	1	0.25
ZF2	1	0.5
ZF3	1	0.75
ZF4	1	1

Characterization

Powder XRD patterns of the ZnO@γ-Fe_2O_3 nanocomposites were recorded using a Bruker AXS D8-Advance X-ray diffractometer with Cu-Kα radiation ($\lambda = 1.5406$ Å) with a scan speed, 2°/min. The acceleration voltage for the XRD analysis was 40 kV and 30 mA with a 2θ interval of 0.018°. A Thermo Nicolet Nexus FT-IR spectrometer was used for recording IR spectra of the nanocomposites in the range 400–4000 cm^{-1} using KBr pellets. Differential thermal analysis (DTA) of the nanocomposites was recorded on an EXSTAR TG/DTA 6300 instrument under air (flow rate = 200 mL/min) from 25 to 800 °C with a heating rate of 10 °C min^{-1}. The morphology and elemental analyses of the core–shell nanocomposites were studied with the help of a field emission scanning electron microscope (Carl Zeiss (ULTRA plus)) operating at an accelerating voltage of 15 kV coupled with an energy dispersive X-ray analysis (EDXA) facility. The transmission electron microscope images, selected area electron diffraction patterns (SAED) and high-resolution transmission electron microscope images (HRTEM) were acquired using a FEI TECNAI G^2 electron microscope

operating at an accelerating voltage of 200 kV. For the TEM measurements, the nanocomposite powders were dispersed in ethanol with the help of a sonicator and a drop each from the dispersions was allowed to dry on carbon-coated copper grids in air. Diffuse reflectance spectra of the nanocomposites were recorded using a Varian Cary 5000 UV–VIS–NIR spectrophotometer attached with a diffuse reflectance accessory. $BaSO_4$ was used as the reference and the spectra were recorded in the range of 300–800 nm. Photoluminescence spectra were recorded with a Shimadzu (RF-5301PC) spectrofluorophotometer with $\lambda_{excitation}$ as 325 nm. The emission spectra of ZnO@γ-Fe_2O_3 core–shell nanocomposites were recorded by dispersing about 5 mg of each nanocomposite powder in 5 mL water followed by sonication for 10 min. Surface area of the nanocomposites was measured using a NOVA 2200e (Quantachrome) instrument by BET method using nitrogen physisorption at 77 K. Prior to the analysis, the samples were degassed at 150 °C for 2 h. Magnetic measurements (M–H curves at 300 and 5 K) of pure γ-Fe_2O_3 nanoparticles and the ZnO@γ-Fe_2O_3 core–shell nanocomposites were carried out on a 3 Tesla cryogen-free mini Vibrating Sample Magnetometer with a pulse cryocooler (CRYOGENICS Ltd, UK). Thermal variation of the magnetization between 5 and 300 K was also studied using the same instrument in the zero-field-cooled/field-cooled (ZFC/FC) mode under an applied magnetic field of 0.05 T.

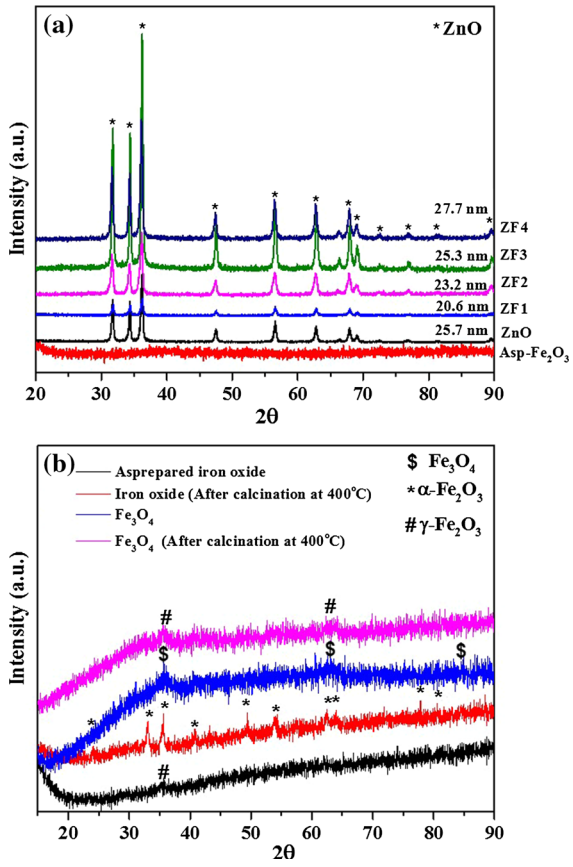

Fig. 1 **a** XRD patterns of ZnO, γ-Fe_2O_3 and ZnO@γ-Fe_2O_3 core–shell nanocomposites (ZF1–ZF4), and **b** XRD patterns of as-prepared iron oxide (prepared by the present thermal decomposition method) and after calcination at 400 °C. The XRD patterns of as prepared Fe_3O_4 nanoparticles and after calcination at 400 °C are also shown

Results and discussion

The XRD patterns of pure iron oxide nanoparticles, ZnO nanorods and ZnO@γ-Fe_2O_3 core–shell nanocomposites (ZF1, ZF2, ZF3 and ZF4) are shown in Fig. 1a. Pure iron oxide nanoparticles do not show any peaks. The XRD patterns of pure ZnO and all the nanocomposites show peaks at 31.7°, 34.2°, 36.1°, 47.6°, 56.5°, 62.7°, 66.3°, 67.7°, 72.5°, 76.9° and 81.5° corresponding to (100), (002), (101), (102), (110), (103), (200), (112), (004), (202), (104) planes of wurtzite ZnO (JCPDS file no. 80-0075). In XRD patterns of the nanocomposites, reflections due to iron oxide are not observed. This is attributed to the presence of very small nanocrystals of γ-Fe_2O_3 that are not detectable by X-ray diffraction. The proof for the presence of γ-Fe_2O_3 comes from XRD, FT-IR, DTA, SAED, and magnetic measurements (discussed latter). The mean crystallite size of pure ZnO and ZnO in the core–shell nanocomposites was estimated using Scherrer equation (Si et al. 2006). The crystallite size of pure ZnO is 25.7 nm and that of ZnO in the nanocomposites varies from 20.6 to 27.7 nm.

To identify the phase of iron oxide nanoparticles prepared by the present thermal decomposition method, Fe_3O_4 nanoparticles were prepared for comparison using a reported method (Ayyappan et al. 2008). Fe^{2+} and Fe^{3+} salts (ferric nitrate and ferrous sulphate) were mixed in distilled water in appropriate proportions and co-precipitated with the help of aqueous ammonia solution at 70 °C. The XRD patterns of as prepared iron oxide prepared by the thermal decomposition method and that of Fe_3O_4

nanoparticles are shown in Fig. 1b. The XRD pattern of as-prepared iron oxide prepared by the thermal decomposition method shows no discernible peaks. The XRD pattern of the same sample after calcination at 400 °C for 3 h shows peaks at 33.1°, 35.4°, 40.7°, 43.3°, 49.5°, 54.1°, 62.4° and 64.1° corresponding to (121), (110), (120), (020), (220), (132), (130) and (211) planes of α-Fe_2O_3 (JCPDS file No. 85-0987). The XRD pattern of Fe_3O_4 nanoparticles, prepared by the reported method, shows weak reflections at 35.5° and 63.1° corresponding to (311) and (440) planes of Fe_3O_4 (JCPDS file no. 85-1436). The XRD pattern of Fe_3O_4 nanoparticles calcined at 400 °C shows weak reflections at 35.6° and 63.8° corresponding to (311) and (440) planes of γ-Fe_2O_3. In general, it is difficult to distinguish γ-Fe_2O_3 and Fe_3O_4 from the XRD patterns. When γ-Fe_2O_3 is heated at 400 °C in air, it transforms to α-Fe_2O_3 and when Fe_3O_4 is heated at 400 °C in air, it transforms to γ-Fe_2O_3 (Ayyappan et al. 2008; Jayanthi et al. 2015; Teja and Koh 2009). Based on the XRD results of samples after calcination, the as-prepared iron oxide nanoparticles, prepared by the present thermal decomposition method, are proposed to be γ-Fe_2O_3 which on calcination transforms to α-Fe_2O_3.

The IR spectra of pure ZnO nanorods and the ZnO@γ-Fe_2O_3 core–shell nanocomposites were recorded (Fig. S1a). Two broad bands at 3434 and 1600 cm^{-1} are attributed to O–H stretching and bending, respectively, due to adsorbed water molecules. The IR bands near 2920 and 2840 cm^{-1} are due to C–H stretching and are attributed to the presence of organic molecules adsorbed on the surface of ZnO@γ-Fe_2O_3 core–shell nanocomposites (Hernández et al. 2007). The band at 1432 cm^{-1} is attributed to stretching vibration of COO^-. The band at 1096 cm^{-1} is due to C–O–C bond (Yang et al. 2015). These observed bands suggest the presence of organic content adsorbed on the surface of the nanocomposites (Yang et al. 2015). The bands at 553 and 453 cm^{-1} are attributed to characteristic absorption of γ-Fe_2O_3 and the band at 444 cm^{-1} is attributed to ZnO (Maiti et al. 2015; Morales et al. 1999). Figure S1b shows the FT-IR spectra for as-prepared iron oxide nanoparticles prepared by the present thermal decomposition method, after calcination at 400 °C and the as-prepared Fe_3O_4 nanoparticles. The as-prepared Fe_2O_3 nanoparticles show IR bands at 453 and 553 cm^{-1} attributed to Fe–O bond of γ-Fe_2O_3 (Maity and Agrawal 2007; Morales et al. 1999). The iron oxide nanoparticles (prepared by the thermal decomposition method) calcined at 400 °C show IR bands at 480 and 549 cm^{-1} attributed to Fe–O bond of α-Fe_2O_3 (Apte et al. 2007; Pandey et al. 2014; Suresh et al. 2014). Fe_3O_4 nanoparticles show characteristic IR bands at 426 and 580 cm^{-1} (Saffari et al. 2015; Song et al. 2015). The as-prepared iron oxide nanoparticles prepared by the thermal decomposition method and after calcination at 400 °C show IR bands at 1390 and 1031 cm^{-1} attributed to the stretching vibration of COO^- and C–O–C, respectively (Yang et al. 2015). These bands are attributed to the presence of organic molecules adsorbed on the surface of iron oxide nanoparticles.

Figure 2 shows the DTA curves for pure ZnO, as-prepared γ-Fe_2O_3 nanoparticles and the ZnO@γ-Fe_2O_3 core–shell nanocomposites. The DTA curve for ZnO does not show any peak. The DTA curve for as-prepared pure γ-Fe_2O_3 nanoparticles shows an exothermic peak at 212 °C which is attributed to the removal of organic content adsorbed on the surface of iron oxide nanoparticles (Hernández et al. 2007; Lee et al. 2008). To verify whether the sharp peak at 212 °C is due to crystallization, the as-prepared iron oxide was calcined at 225 °C for 3 h and XRD pattern was recorded for the calcined sample. The XRD pattern did not show any discernible peak indicating that the sharp peak in the DTA pattern at 212 °C is not due to crystallization. The ZnO@γ-Fe_2O_3 core–shell

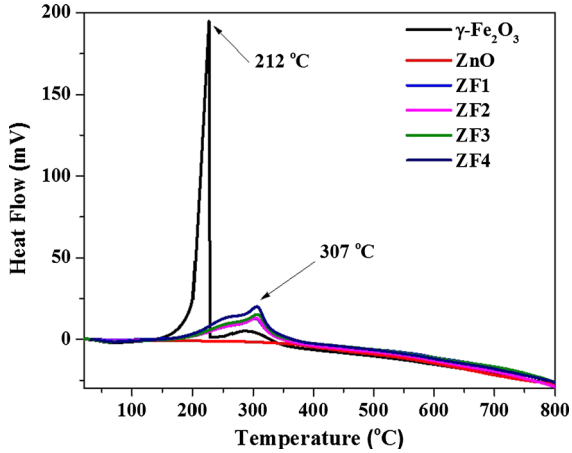

Fig. 2 DTA curves for pure γ-Fe_2O_3 nanoparticles, ZnO and the ZnO@γ-Fe_2O_3 core–shell nanocomposites (ZF1, ZF2, ZF3 and ZF4)

nanocomposites show broad exothermic hump from 200 to 250 °C which is attributed to the removal of organic content adsorbed on the surface of ZnO@γ-Fe_2O_3 core–shell nanocomposites. The DTA curves for as prepared iron oxide nanoparticles and all the ZnO@γ-Fe_2O_3 core–shell nanocomposites show a broad exothermic hump from 250 to 360 °C attributed to the phase transition of γ-Fe_2O_3 to α-Fe_2O_3 (Phu et al. 2011; Schimanke and Martin 2000; Yu et al. 2013). Phu et al. have reported DTA results for the phase transition of γ-Fe_2O_3 to α-Fe_2O_3 in the temperature range of 310–360 °C (Phu et al. 2011). Schimanke and Martin have reported phase transition of γ-Fe_2O_3 to α-Fe_2O_3, based on DTA results in the range from 290 to 400 °C (Schimanke and Martin 2000). Yu et al. have reported TG/DSC results, suggesting phase transition of γ-Fe_2O_3 to α-Fe_2O_3 in the range from 200 to 500 °C (Yu et al. 2013). From the DTA results, it is evident that the as-prepared iron oxide is γ-Fe_2O_3 and, when it is heated in air, it transforms to α-Fe_2O_3 as reported (Azizi and Heydari 2014; Chen and Xu 1998; Phu et al. 2011; Schimanke and Martin 2000; Yu et al. 2013). The DTA results are in accordance with the XRD and FT-IR results.

FE-SEM and TEM measurements were performed to investigate morphology and size of ZnO, γ-Fe_2O_3 and the ZnO@γ-Fe_2O_3 core–shell nanocomposites. Figure 3 shows the FE-SEM images of pure ZnO, γ-Fe_2O_3 nanoparticles and the ZnO@γ-Fe_2O_3 core–shell nanocomposites (ZF1–ZF4). Pure ZnO exhibits nanorods and γ-Fe_2O_3 shows small agglomerated nanoparticles. After the deposition of γ-Fe_2O_3, the shape of ZnO is retained but the surface of ZnO nanorods is not smooth. Nanocomposites ZF1 and ZF2 show uniform shell formation of γ-Fe_2O_3 over the ZnO nanorods. Nanocomposites ZF3 and ZF4 show formation of γ-Fe_2O_3 shell over the ZnO nanorods with aggregation. The aggregation of γ-Fe_2O_3 nanoparticles increases as one increases the amount of $Fe(acac)_3$ used during the synthesis of the core–shell nanocomposites (ZF1–ZF4). Table 2 shows EDX analysis results on the ZnO@γ-Fe_2O_3 core–shell nanocomposites. The nanocomposites ZF1, ZF2 and ZF4 show uniform elemental distribution as compared to nanocomposite ZF3.

Figure 4 shows the TEM images and high resolution TEM (HRTEM) images of ZnO and γ-Fe_2O_3 nanoparticles. ZnO nanorods (Fig. 4a) are 1.1 ± 0.1 μm in length and 40.1 ± 7 nm in width. The SAED pattern of ZnO (inset of Fig. 4a) shows spots attributed to (101), (103), (202), (004) and (002) planes of wurtzite ZnO (JCPDS file no. 80-0075). Figure 4b shows small γ-Fe_2O_3 nanoparticles (2.1 ± 0.3 nm) and the SAED pattern (inset of Fig. 4b) shows rings attributed to (311), (421) and (440) planes of γ-Fe_2O_3 (JCPDS file no. 39-1346). The HRTEM images of pure ZnO nanorod (Fig. 4c) and γ-Fe_2O_3 nanoparticles (Fig. 4d) exhibit interplanar spacing of 0.24 and 0.48 nm which are attributed to (101) plane of ZnO and (111) plane of γ-Fe_2O_3, respectively.

The TEM and HRTEM images of ZnO@γ-Fe_2O_3 core–shell nanocomposites ZF1 and ZF2 are shown in Fig. 5. The ZnO@γ-Fe_2O_3 core–shell nanocomposites ZF1 (Fig. 5a) and ZF2 (Fig. 5c) show formation of uniform γ-Fe_2O_3 shell on the surface of ZnO nanorods. The inset of Fig. 5a shows the TEM image of a single nanorod of core–shell nanocomposite ZF1 coated uniformly with a shell of γ-Fe_2O_3 (∼15 nm). The HRTEM image of nanocomposite ZF1 (Fig. 5b) shows interplanar spacing values of 0.24 and 0.48 nm for the core and shell regions corresponding to ZnO (101) and γ-Fe_2O_3 (111) planes, respectively. This indicates that the γ-Fe_2O_3 shell with (111) plane is deposited on crystalline ZnO nanorod core with (101) plane. The inset of Fig. 5c shows the TEM image of a single nanorod of core–shell nanocomposite ZF2 coated uniformly with γ-Fe_2O_3 shell (∼20 nm). The HRTEM image of core–shell nanocomposite ZF2 (Fig. 5d) exhibits 0.24 nm as interplanar spacing attributed to (101) plane of ZnO.

Figure 6 shows the TEM and HRTEM images of ZnO@γ-Fe_2O_3 core–shell nanocomposites ZF3 and ZF4. The core–shell nanocomposites ZF3 (Fig. 6a) and ZF4 (Fig. 6c) show formation of γ-Fe_2O_3 shell on the ZnO nanorods. The insets of Fig. 6a, c show the TEM images of single nanorods of the core–shell nanocomposites coated with γ-Fe_2O_3 shell of thickness 10 nm (ZF3) and 15 nm (ZF4). The HRTEM image of core–shell nanocomposite ZF3 (Fig. 6b) exhibits 0.24 nm as interplanar spacing attributed to (101) plane of ZnO and the HRTEM image of core–shell nanocomposite ZF4 (Fig. 6d) exhibits interplanar spacing values of 0.24 and 0.48 nm for the core and shell regions corresponding to ZnO (101) and γ-Fe_2O_3 (111) planes, respectively. This again indicates that γ-

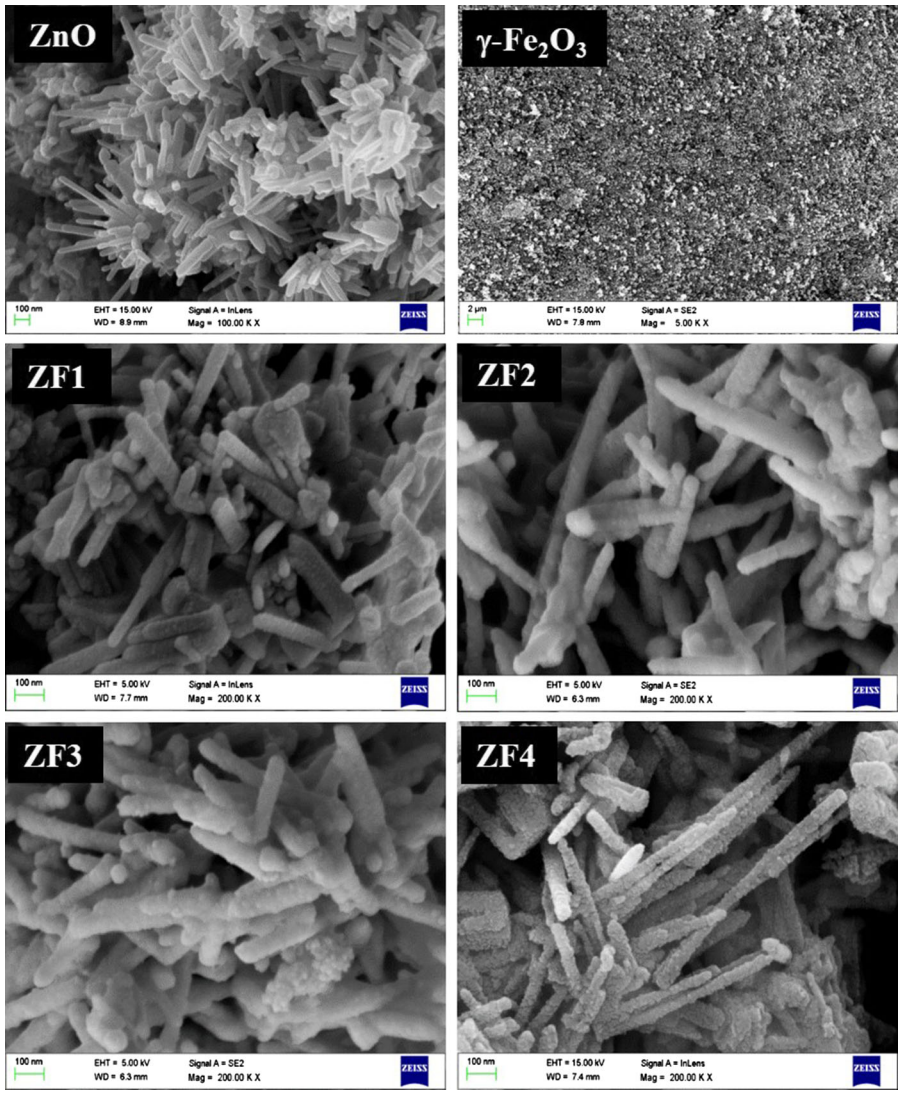

Fig. 3 FE-SEM images of ZnO nanorods, γ-Fe_2O_3 nanoparticles and ZnO@ γ-Fe_2O_3 core–shell nanocomposites (ZF1, ZF2, ZF3 and ZF4)

Fe_2O_3 shell with (111) plane is deposited on crystalline ZnO nanorods (core) with (101) plane.

The SAED patterns of core–shell nanocomposites ZF1, ZF2, ZF3 and ZF4 are shown in Fig. S2. The SAED patterns of nanocomposites ZF1–ZF3 (Fig. S2a–c) show spots which are attributed to (101), (102), (103), (002) and (004) planes of hexagonal ZnO and rings due to (311), (440) and (310) planes of γ-Fe_2O_3. The SAED pattern of nanocomposite ZF4 (Fig. S2d) shows spots which are attributed to (101), (110), (103), (201) and (202) planes of hexagonal ZnO and rings due to (311), (440), (321) planes of γ-Fe_2O_3.

Diffuse reflectance spectra of pure ZnO nanorods, γ-Fe_2O_3 nanoparticles (before calcination) and the ZnO@γ-Fe_2O_3 core–shell nanocomposites (ZF1, ZF2, ZF3 and ZF4) are shown in Fig. 7. ZnO shows absorption in the UV region at about 385 nm. Pure γ-Fe_2O_3 nanoparticles show absorption at about 653 nm. The ZnO@γ-Fe_2O_3 core–shell nanocomposites show an extended optical absorption in the visible region. One can observe two absorption bands in the

Table 2 EDX analysis data for the ZnO@γ-Fe_2O_3 core–shell nanocomposites (ZF1–ZF4). The analysis was done at three different spots

Nanocomposite	Zn		Fe		O		Comment
	Wt%	At.%	Wt%	At.%	Wt%	At.%	
ZF1	70.3	40.2	2.6	2.7	20.8	56.1	Uniform
	71.2	40.8	2.5	2.6	20.5	50.5	
	70.8	40.4	2.2	2.9	21.1	58.7	
ZF2	71.9	41.2	3.8	3.6	23.2	54.8	Uniform
	71.4	41.9	3.4	3.9	23.3	55.1	
	71.8	40.8	3.5	3.7	23.6	55.5	
ZF3	78.4	55.1	3.9	3.9	14.6	40.9	Non-uniform
	80.8	56.3	5.0	3.9	16.2	43.8	
	81.6	57.1	4.7	3.9	13.6	38.9	
ZF4	78.8	51.5	4.3	3.3	16.9	45.2	Uniform
	78.8	50.2	4.8	3.1	18.3	47.6	
	79.7	52.3	4.5	2.9	16.8	45.0	

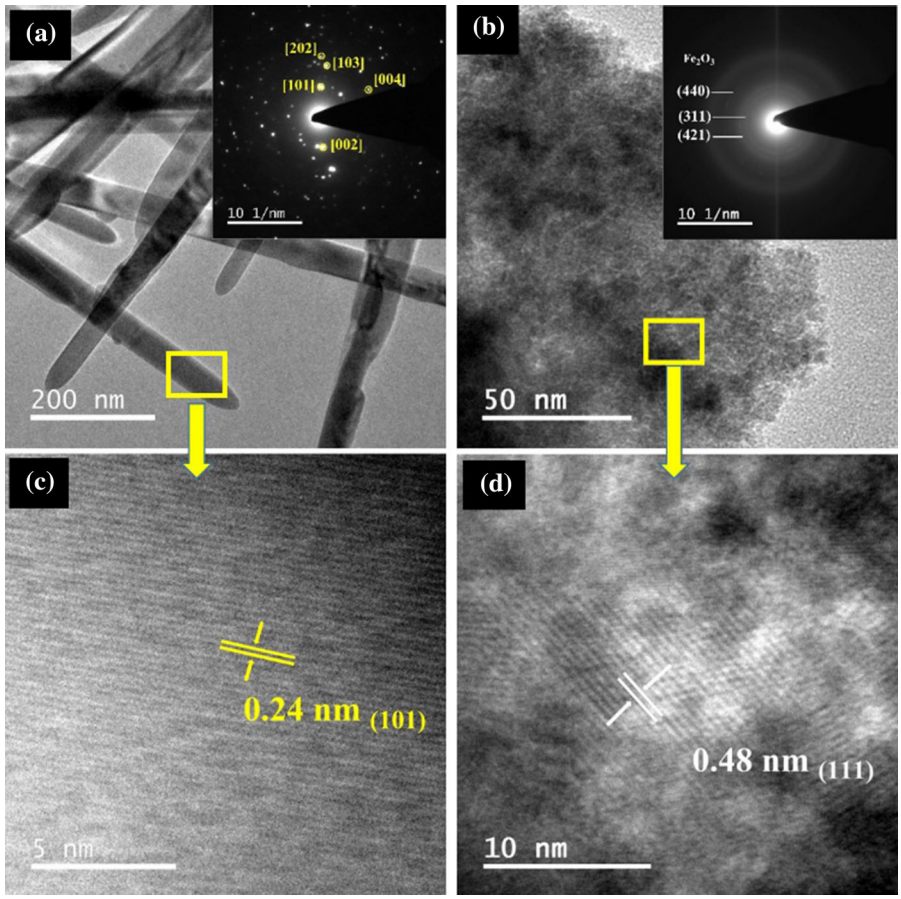

Fig. 4 TEM images of **a** ZnO nanorods, **b** γ-Fe_2O_3 nanoparticles, **c** HRTEM image of ZnO nanorods and **d** HRTEM image of γ-Fe_2O_3 nanoparticles

diffuse reflectance spectra of the ZnO@γ-Fe_2O_3 core–shell nanocomposites. The first one is observed at low energy in the visible region (between 550 and 655 nm) which is due to the absorption of γ-Fe_2O_3. The second absorption (at about 380 nm) is attributed to the absorption of ZnO.

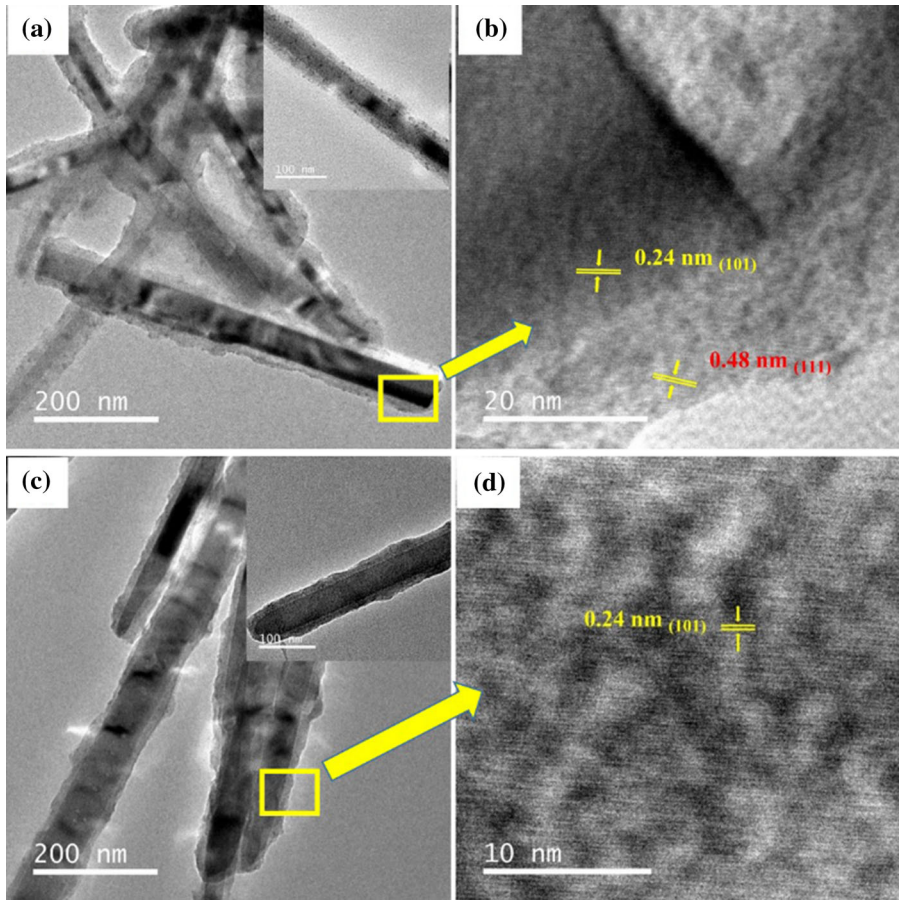

Fig. 5 TEM and HRTEM images of ZnO@γ-Fe_2O_3 core–shell nanocomposites; ZF1 (**a**, **b**), and ZF2 (**c**, **d**)

The absorption of ZnO@γ-Fe_2O_3 core–shell nanocomposites in the visible region increases with an increase in the concentration of precursor for γ-Fe_2O_3 (i.e. $Fe(acac)_3$) used during the synthesis of the nanocomposites. The band gap of ZnO nanorods, γ-Fe_2O_3 nanoparticles and ZnO@γ-Fe_2O_3 core–shell nanocomposites was estimated by plotting $(\alpha hv)^2$ versus hv (Tauc plots) using the relation Chen et al. (2010b):

$$\alpha hv = A\left(hv - E_g\right)^{1/2}$$

where α is the absorption coefficient, hv is the photon energy, E_g is the optical band gap energy and A is a constant. From the Tauc plots (Fig. S3), E_g was estimated by extrapolating a straight line from the linear portion of the absorption curve to the X-axis. The band gap values of pure ZnO nanorods and pure γ-Fe_2O_3 nanoparticles are 3.2 and 1.9 eV, respectively. Band gap values of 2.24, 2.2, 2.18 and 1.9 eV due to γ-Fe_2O_3 are observed for the ZnO@γ-Fe_2O_3 core–shell nanocomposites ZF1, ZF2, ZF3 and ZF4, respectively. The insets of Tauc plots (Fig. S3) of ZnO@γ-Fe_2O_3 core–shell nanocomposites (ZF1, ZF2, ZF3 and ZF4) show band gap of 3.3 eV due to ZnO. The band gap of γ-Fe_2O_3 in the core–shell nanocomposites shows red shift from ZF1 to ZF4. This red shift is attributed to an increase in particle size of γ-Fe_2O_3 with an increase in the precursor concentration of γ-Fe_2O_3 (i.e. $Fe(acac)_3$) used during the synthesis of the ZnO@γ-Fe_2O_3 nanocomposites (Hernández et al. 2007; Yin et al. 2014).

The UV–Visible absorption spectra of pure ZnO nanorods, iron oxide nanoparticles (as prepared by the thermal decomposition method, calcined at 400 °C and Fe_3O_4) and the ZnO@γ-Fe_2O_3 core–shell nanocomposite ZF1 are shown in Fig. S4. The spectra were recorded using dispersions in ethanol. The absorption spectrum of ZnO shows band edge absorption at about 376 nm (3.3 eV) which is blue shifted

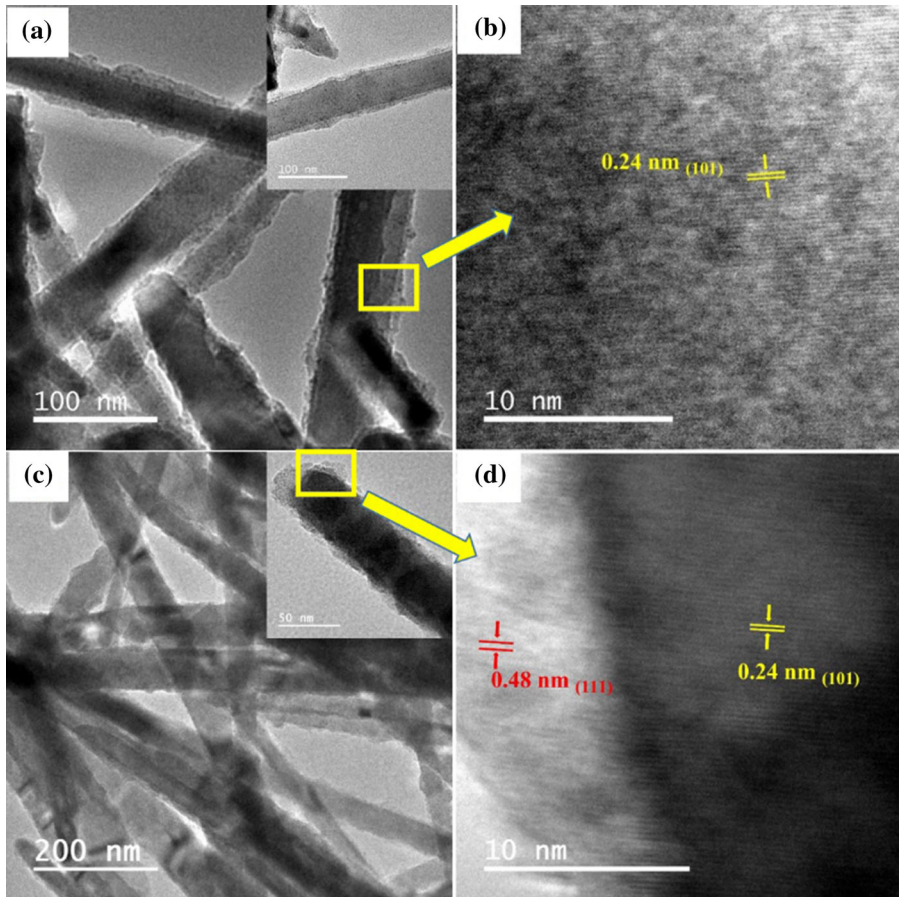

Fig. 6 TEM and HRTEM images of ZnO@γ-Fe_2O_3 core–shell nanocomposites; ZF3 (**a**, **b**), and ZF4 (**c**, **d**)

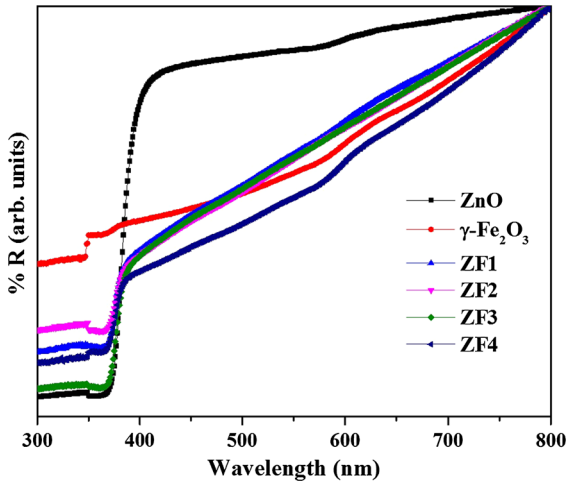

Fig. 7 Diffuse reflectance spectra of ZnO nanorods, as-prepared γ-Fe_2O_3 nanoparticles (before calcination) and the ZnO@γ-Fe_2O_3 core–shell nanocomposites (ZF1–ZF4)

from that of bulk ZnO (3.2 eV) due to quantum confinement (Hernández et al. 2007). The as-prepared iron oxide nanoparticles (prepared by the thermal decomposition method) show absorption in the visible region (400–800 nm) with a broad band at about 440 nm which corresponds to that of γ-Fe_2O_3 nanoparticles (Wu and Wang 2014). The absorption spectrum of γ-Fe_2O_3 nanoparticles calcined at 400 °C shows absorption at about 575 nm characteristic of α-Fe_2O_3 (Pandey et al. 2014; Suresh et al. 2014). Fe_3O_4 nanoparticles show band edge absorption at about 503 nm (Wu and Wang 2014). The absorption spectrum of ZnO@γ-Fe_2O_3 core–shell nanocomposite ZF1 shows a small shoulder at about 565 nm and a band edge absorption at about 376 nm (3.3 eV) attributed to γ-Fe_2O_3 and ZnO, respectively (Hernández et al. 2007; Reda 2010; Zhang et al. 1997). The UV–Vis spectral studies also suggest that the phase of as-

prepared iron oxide nanoparticles, prepared by the thermal decomposition method, is γ-Fe_2O_3.

Figure 8 shows the photoluminescence spectra of pure ZnO nanorods, γ-Fe_2O_3 nanoparticles prepared by the thermal decomposition method (before calcination) and the ZnO@γ-Fe_2O_3 core–shell nanocomposites (ZF1, ZF2, ZF3 and ZF4). The PL spectra of pure ZnO and ZnO@γ-Fe_2O_3 core–shell nanocomposites show emission bands around 382 and 469 nm. The emission band at about 382 nm is due to band-edge emission of ZnO. The broad emission centred at 469 nm, observed in ZnO nanorods, γ-Fe_2O_3 nanoparticles and all the core–shell nanocomposites (ZF1, ZF2, ZF3 and ZF4), is attributed to the presence of oxygen vacancies and defects (Liu et al. 2012). In the ZnO@γ-Fe_2O_3 core–shell nanocomposites, the defect emission at 469 nm is enhanced as compared to pure ZnO nanorods and γ-Fe_2O_3 nanoparticles. A possible reason is reduction in the number of hydroxyls groups on the surface of ZnO nanorods due to the formation of γ-Fe_2O_3 shell. Depletion of hydroxyls groups is known to increase oxygen vacancies and surface defects on the surface of ZnO nanorods (Chu et al. 2008). The oxygen vacancies/defects are good electron scavengers and thus expected to improve the photocatalytic activity (Abdullah Mirzaie et al. 2012). The defect emission decreases in the ZnO@γ-Fe_2O_3 core–shell nanocomposites from ZF1 to ZF4 with an increase in the concentration of $Fe(acac)_3$, used during the preparation of the core–shell nanocomposites. The presence of more and more γ-Fe_2O_3 nanoparticles on the surface of ZnO nanorods due to increase in the concentration of $Fe(acac)_3$, used during the synthesis, decreases surface defects and oxygen vacancies on the surface of ZnO nanorods (Wu et al. 2010).

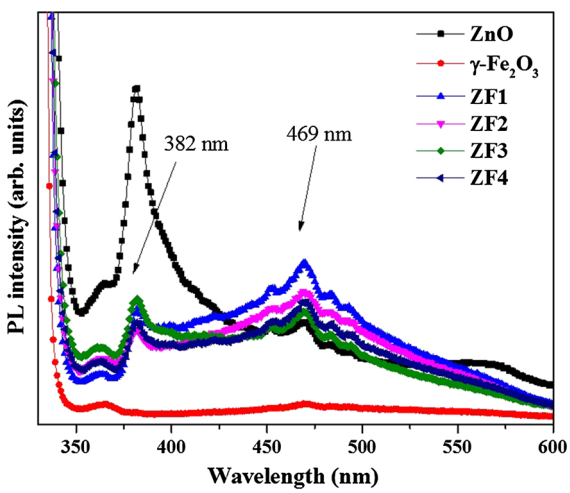

Fig. 8 Photoluminescence spectra of ZnO nanorods, γ-Fe_2O_3 nanoparticles (prepared by the thermal decomposition method) and the ZnO@γ-Fe_2O_3 core–shell nanocomposites (ZF1, ZF2, ZF3 and ZF4)

Magnetic measurements were carried out for pure γ-Fe_2O_3 nanoparticles, prepared by the present thermal decomposition method, and the ZnO@γ-Fe_2O_3 core–shell nanocomposites. Magnetic measurements were done only for those nanocomposites which exhibited uniform elemental distribution (ZF1, ZF2 and ZF4). Nanocomposite ZF3 did not exhibit uniform elemental distribution (see Table 2 on EDXA results). The magnetization versus magnetic field (M–H) plots for pure γ-Fe_2O_3 nanoparticles and the core–shell nanocomposites (ZF1, ZF2 and ZF4) are shown in Fig. 9. All the samples exhibit superparamagnetic behaviour at 300 K. At 5 K, however, the samples exhibit weak ferromagnetic behaviour with small coercivity (H_c) and remanent magnetization (M_r). In general, for a superparamagnetic system, the coercivity and remanent magnetization increases below the superparamagnetic–ferromagnetic transition (Wilson et al. 2004; Zhang et al. 1997). The observed magnetic behaviour and magnetic parameters for pure γ-Fe_2O_3 nanoparticles and ZnO@γ-Fe_2O_3 core–shell nanocomposites are summarized in Table 3. The coercivity of pure γ-Fe_2O_3 nanoparticles (0.05 T), and the core–shell nanocomposites ZF2 (0.055 T) and ZF1 (0.05 T) are almost the same. The coercivity of core–shell nanocomposite ZF4 (0.045 T) is less than that of pure γ-Fe_2O_3, ZF1 and ZF2. This is attributed to an increase in the particle size of iron oxide nanoparticles in the nanocomposite ZF4 (Lin et al. 2006). Remanent magnetization values for the nanocomposites ZF1, ZF2 and ZF4 are 0.38, 0.88 and 0.66 emu/g, respectively. Remanent magnetization is lower in all the core–shell nanocomposites as compared to that of pure γ-Fe_2O_3 nanoparticles (2.7 emu/g). This is attributed to the presence of diamagnetic ZnO nanorods, which decreases the effective mass of iron oxide (Zhang et al. 2013). The unexpectedly high remanent magnetization in case of nanocomposite ZF2 is attributed to the formation of thicker shell of iron oxide (∼20 nm) over ZnO nanorods as compared to the other nanocomposites (ZF1 and ZF4) (Ma et al. 2015). At 300 K, the saturation magnetization (M_s) values of the core–shell

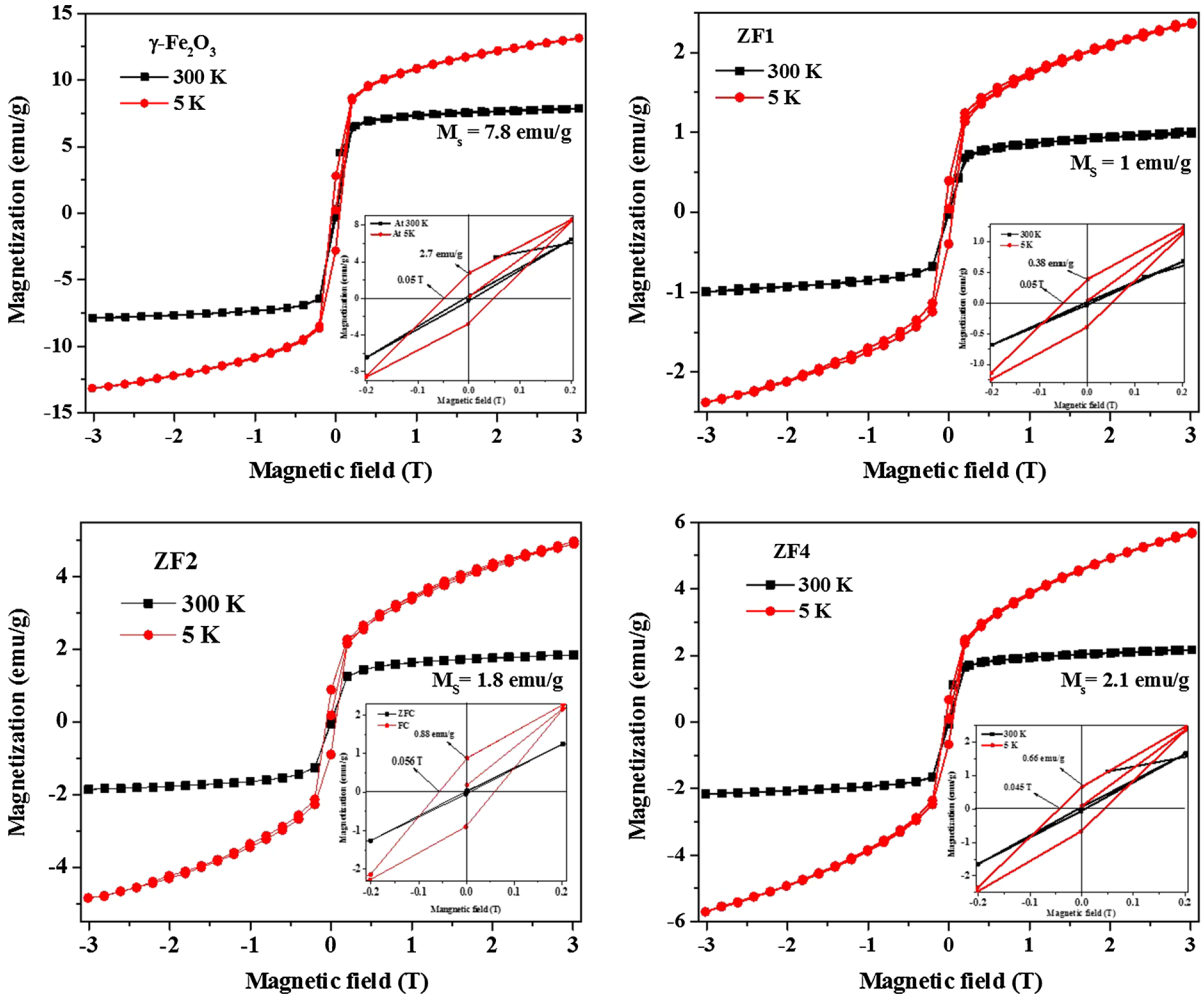

Fig. 9 M–H curves of pure γ-Fe_2O_3 nanoparticles, prepared by thermal decomposition method, and the core–shell nanocomposites (ZF1, ZF2 and ZF4)

Table 3 Magnetic parameters for pure iron oxide nanoparticles and ZnO@γ-Fe_2O_3 core–shell nanocomposites

Sample	H_c (T)		M_r (emu/g)		M_s (emu/g)		T_B (K)	T_M (K)	Particle size of γ-Fe_2O_3 estimated from T_B (nm)
	5 K	300 K	5 K	300 K	5 K	300 K			
γ-Fe_2O_3	0.05	–	2.7	–	–	7.8	43	266	18.2
ZF1	0.05	–	0.38	–	–	1.0	30	265	16.2
ZF2	0.055	–	0.88	–	–	1.8	45	266	18.5
ZF4	0.045	–	0.66	–	–	2.1	55	260	19.8

nanocomposites are less than that of γ-Fe_2O_3 nanoparticles and bulk maghemite (76 emu/g). The decrease of M_s in the core–shell nanocomposites is attributed to the presence of diamagnetic ZnO, surface spin disorder and canting (Wilson et al. 2004; Zhang et al. 2013). The saturation magnetization increases with an

increase in the iron content of the nanocomposites ZF1–ZF4 (Table 3). In addition, there is an increase in the particle size of γ-Fe_2O_3 nanoparticles in the core–shell nanocomposites with an increase in the concentration of precursor for iron oxide ($Fe(acac)_3$) used during the synthesis (Kishore and Jeevanadam 2011). Figure 9 reveals that the magnetization at 5 K does not saturate for the as-prepared pure γ-Fe_2O_3 nanoparticles and also for the core–shell nanocomposites at 3 T. This is attributed to frozen spins on the surface as has been reported for maghemite nanoparticles (Balti et al. 2014; Nadeem et al. 2011).

The zero-field-cooled (ZFC) and field-cooled (FC) magnetization curves for the as-prepared pure γ-Fe_2O_3 nanoparticles and for the ZnO@γ-Fe_2O_3 core–shell nanocomposites (ZF1, ZF2 and ZF4), under an applied field of 0.05 T, are shown in Fig. 10. Pure γ-Fe_2O_3 nanoparticles and the core–shell nanocomposites (ZF1, ZF2 and ZF4) show broad maxima in the ZFC curves (Table 3). The temperature corresponding to the broad maxima is called as the blocking temperature (T_B), and it corresponds to the superparamagnetic transition of iron oxide nanoparticles.

At temperatures higher than T_B, the magnetization decreases and follows a Curie–Weiss law (Liu and Ma 2015). The observed blocking temperature for pure γ-Fe_2O_3 nanoparticles is 43 K and for the core–shell nanocomposites ZF1, ZF2 and ZF4, the T_B values are 30, 45 and 55 K, respectively. The increase in the blocking temperature in the nanocomposites ZF2 and ZF4 compared to ZF1 is attributed to an increase in dipolar interaction due to increase in the particle

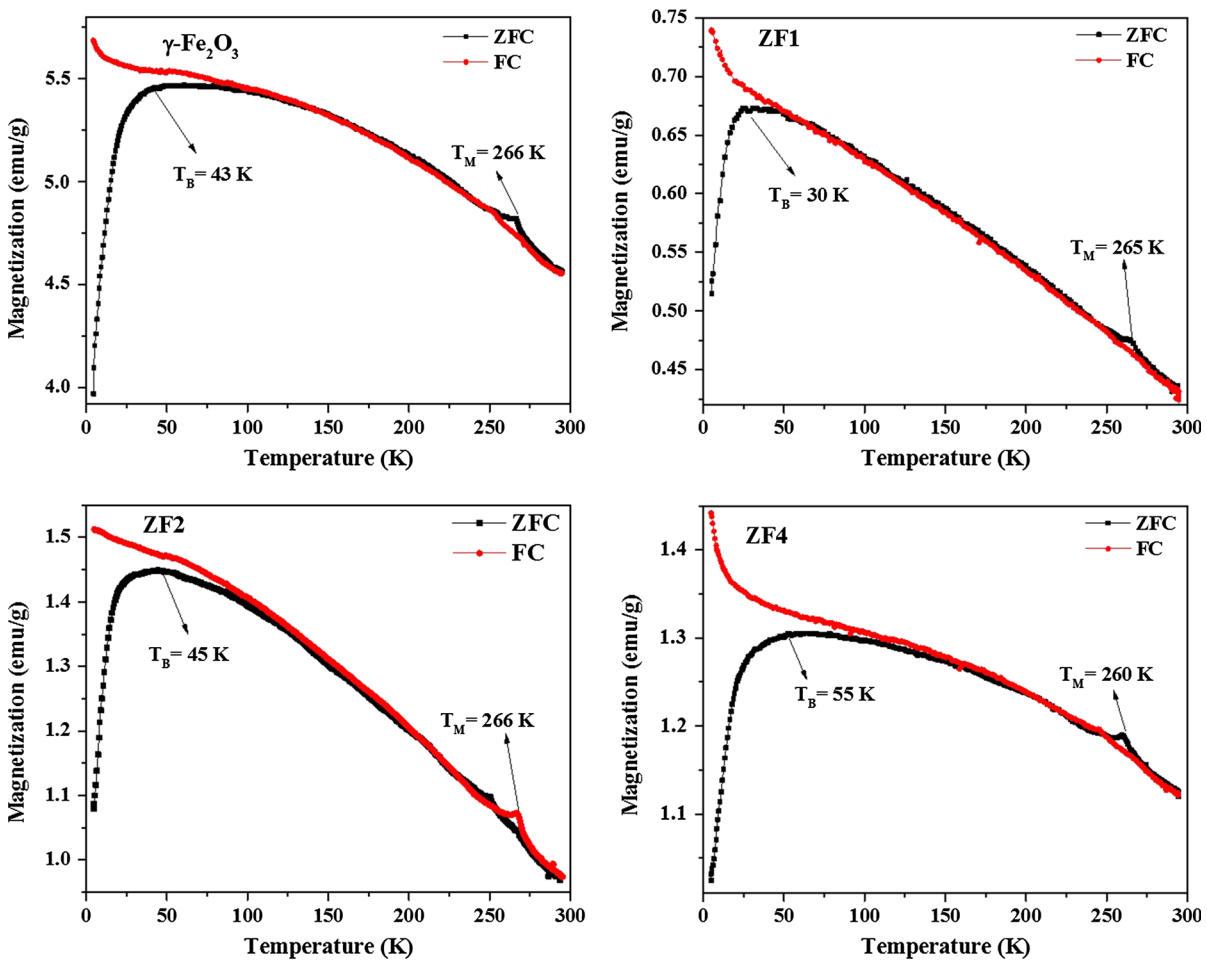

Fig. 10 ZFC and FC curves of pure γ-Fe_2O_3 nanoparticles, prepared by thermal decomposition method, and ZnO@γ-Fe_2O_3 core–shell nanocomposites (ZF1, ZF2 and ZF4)

volume (Mikhaylova et al. 2004). The broad maxima in the ZFC curves of γ-Fe_2O_3 nanoparticles and the core–shell nanocomposites (ZF1, ZF2 and ZF4) indicate broad particle size distribution of iron oxide nanoparticles (Kishore and Jeevanadam 2011). The particle volume (V) can be calculated from T_B using the following equation (Laurent et al. 2008).

$$T_B = \frac{K_{\text{eff}} V}{25 k_B}$$

where K_{eff} is the effective anisotropy constant (for bulk γ-Fe_2O_3, $K_{\text{eff}} = 4.7 \times 10^4$ erg cm^{-3}) and k_B is the Boltzmann constant. The average particle sizes of γ-Fe_2O_3 calculated from the T_B of pure γ-Fe_2O_3 nanoparticles and the core–shell nanocomposites ZF1, ZF2, ZF4 are 18.2, 16.2, 18.5 and 19.8 nm, respectively. The ZFC curves of pure γ-Fe_2O_3 and nanocomposites ZF1, ZF2 and ZF4 also show Morin transition at about 266, 265, 266 and 260 K, respectively. The observation of Morin transition is attributed to the presence of a small amount of α-Fe_2O_3 nanoparticles due to the structural transformation of γ-Fe_2O_3 into α-Fe_2O_3 nanoparticles (Mashlan et al. 2004). In α-Fe_2O_3, Morin transition is a phase transition in which a weakly ferromagnetic state converts into an antiferromagnetic state (Mukherjee et al. 2008).

Figure S5 shows M–H curves for as prepared iron oxide nanoparticles prepared by the thermal decomposition method followed by calcination at 400 °C (i.e. α-Fe_2O_3), ZnO@γ-Fe_2O_3 core–shell nanocomposite ZF1 calcined at 400 °C, and Fe_3O_4 nanoparticles prepared by the reported method (before calcination). The observed magnetic parameters such as coercivity (H_c), remanent magnetization (M_r) and saturation magnetization (M_s) have been summarized in Table 4. Pure γ-Fe_2O_3 nanoparticles calcined at 400 °C show weak ferromagnetic behaviour at both 300 and 5 K with H_c values 0.016 and 0.65 T, respectively. The magnetization does not saturate at both the temperatures at a maximum field of 3 Tesla. The magnetic behaviour of γ-Fe_2O_3 nanoparticles calcined at 400 °C is similar to that reported for α-Fe_2O_3 nanoparticles (Bødker et al. 2000; Jayanthi et al. 2015; Pandey et al. 2014). The core–shell nanocomposite ZF1 (after calcination at 400 °C) shows superparamagnetic behaviour at room temperature. At 5 K, it shows weak ferromagnetic behaviour with a H_c value of 0.1 T. The M–H curves of Fe_3O_4 nanoparticles show superparamagnetic behaviour at

Table 4 Magnetic parameters of as prepared iron oxide nanoparticles prepared by thermal decomposition method, followed by calcination at 400 °C, Fe_3O_4 nanoparticles and core–shell nanocomposite ZF1 (calcined at 400 °C)

Sample	H_c (T)		M_r (emu/g)		T_B (K)	T_M (K)	M_s (emu/g)		Particle size (estimated from T_B) (nm)
	5 K	300 K	5 K	300 K			300 K	5 K	
As prepared iron oxide nanoparticles (thermal decomposition method) followed by calcination at 400 °C	0.65	0.016	4.9	0.95	200	–	–	–	19.5
ZnO@γ-Fe_2O_3 nanocomposite ZF1 (400 °C)	0.1	–	0.8	–	52.5	262	–	–	30.4
Fe_3O_4 nanoparticles	0.48	–	21.4	–	39	–	73	89	17.6

room temperature and weak ferromagnetic behaviour at 5 K with H_c and M_r values of 0.48 T and 21.4 emu/g, respectively. The saturation magnetization values for Fe_3O_4 nanoparticles at 300 and 5 K are 73 and 89 emu/g, respectively.

The ZFC/FC curves of γ-Fe_2O_3 nanoparticles, prepared by the thermal decomposition method, followed by calcination at 400 °C, ZnO@γ-Fe_2O_3 core–shell nanocomposite ZF1 calcined at 400 °C, and Fe_3O_4 nanoparticles are shown in Fig. S6. The ZFC curve for γ-Fe_2O_3 nanoparticles calcined at 400 °C (Fig. S6a) shows a broad maximum around 200 K, corresponding to the blocking temperature. The FC curve departs from the ZFC curve at T_{irr} (blocking temperature of the largest particle) and the magnetization remains constant with decrease in temperature and this is due to strong inter-particle interaction (Sreeja and Joy 2007). The ZFC curve for the ZnO@γ-Fe_2O_3 core–shell nanocomposite ZF1 calcined at 400 °C (Fig. S6b) shows peak at about 52.5 K indicating the superparamagnetic blocking transition. Also, the ZFC curve shows a small hump at 262 K due to Morin transition indicating the formation of α-Fe_2O_3. Pure γ-Fe_2O_3 nanoparticles prepared by the thermal decomposition method and calcined at 400 °C do not show Morin transition. According to Zysler et al. (Zysler et al. 2001), when iron oxide is prepared in the form of small particles, Morin transition is a complicated phenomenon due to the presence of strain and defects. The Morin transition temperature reduces as the particle size decreases and vanishes for iron oxide particles smaller than 8-20 nm (Amin and Arajs 1987). The particle size values of iron oxide nanoparticles, prepared by the thermal decomposition method followed by calcination at 400 °C, and the ZnO@γ-Fe_2O_3 core–shell nanocomposite ZF1 calcined at 400 °C, estimated from their blocking temperatures, are 19.5 nm and 30.4 nm, respectively.

The ZFC curve for Fe_3O_4 nanoparticles (Fig. S6c) shows a broad maximum around 39 K due to superparamagnetic blocking temperature. The particle size of Fe_3O_4 nanoparticles, calculated from the blocking temperature, is 17.6 nm. In general, the saturation magnetization at room temperature reported for γ-Fe_2O_3 nanoparticles is between 1.3 and 69.6 emu/g (Balti et al. 2014; Chu et al. 2008; Morales et al. 1999; Wu et al. 2010; Zhang et al. 2013) and for Fe_3O_4 nanoparticles, the M_s value is between 20 and 84 emu/g (Chen et al. 2010b; Chu et al. 2008; Si et al. 2005). The reported coercivity at 5 K for γ-Fe_2O_3 nanoparticles is between 0.005 and 0.413 T (Tsuzuki et al. 2011; Zysler et al. 2001) and for Fe_3O_4 nanoparticles, the value is between 0.01 and 0.058 T (Saffari et al. 2015; Wu et al. 2015). The reported remanent magnetization values at 5 K for γ-Fe_2O_3 nanoparticles are between 0.62 emu/g and 16.7 emu/g (Woo et al. 2004) and for Fe_3O_4 nanoparticles, the values are between 13 and 18.8 emu/g (Jayanthi et al. 2015; Woo et al. 2004). From the above results, one can conclude that there is difference in the magnetic properties of γ-Fe_2O_3 and Fe_3O_4 nanoparticles. In spite of having nearly the same particle size for the as-prepared iron oxide nanoparticles prepared by the thermal decomposition method (18.2 nm) and Fe_3O_4 nanoparticles (17.6 nm), there is difference in their magnetic behaviour. For the as-prepared iron oxide nanoparticles, the coercivity ($H_c = 0.05$ T) and remanent value ($M_r = 2.7$ emu/g) at 5 K and saturation magnetization ($M_s = 7.8$ emu/g) at room temperature are less than that of Fe_3O_4 nanoparticles ($H_c = 0.48$ T, $M_r = 21.4$ emu/g and $M_s = 73$ emu/g). This suggests that the phase of as-prepared iron oxide nanoparticles, prepared by the present thermal decomposition method, is γ-Fe_2O_3.

ZnO nanorods possess hydroxyl groups on their surface (Chandraiahgari et al. 2015). During the formation of ZnO@γ-Fe_2O_3 core–shell nanocomposites, iron (III) acetylacetonate interacts with the surface of ZnO via hydrogen bonding between the π-system of acetyl acetone and protons of the hydroxyl groups present on the surface of ZnO (Scheme 1). Iron (III) acetylacetonate decomposes in air, at about 200 °C, to produce iron oxide nanoparticles (maghemite) with by-products (Kishore and Jeevanandam 2012).

$$4(C_5H_7O_2)_3Fe + 17O_2 \xrightarrow{\sim 200\,^{\circ}C} 2\gamma\text{-}Fe_2O_3 + 30CO + 10CO_2 + 20CH_4 + 2H_2O$$

Since the thermal decomposition is carried out at 200 °C in diphenyl ether in the presence of ZnO nanorods, ZnO@γ-Fe_2O_3 core–shell nanocomposites are produced.

In order to study the photocatalytic activity of ZnO nanorods, γ-Fe_2O_3 nanoparticles and the ZnO@γ-Fe_2O_3 core–shell nanocomposites, photodegradation of congo red in an aqueous solution under sunlight was

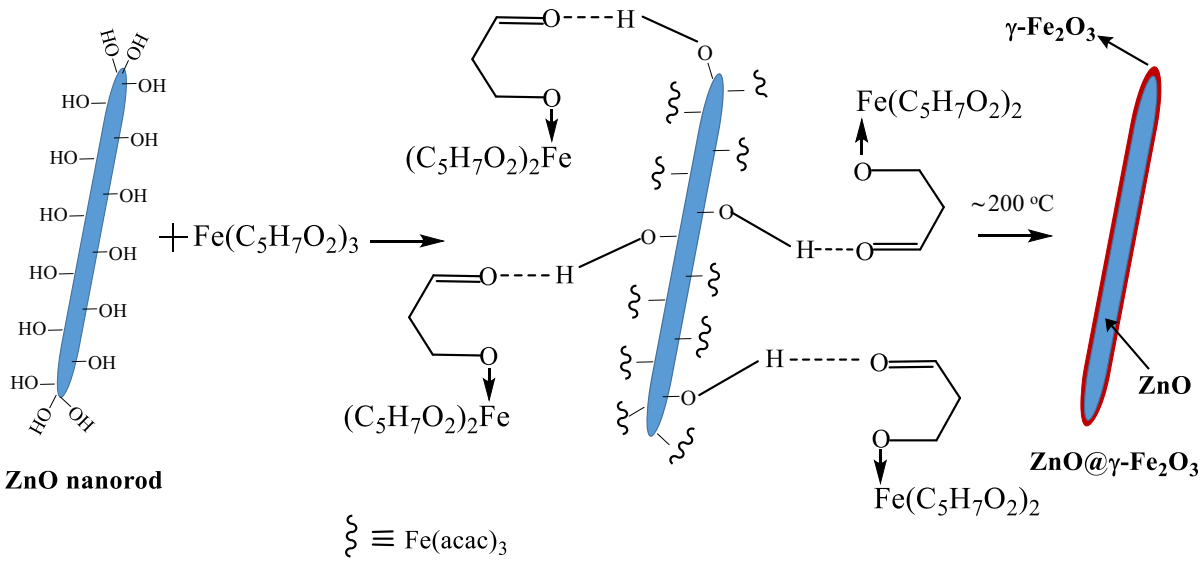

Scheme 1 Attachment of iron (III) acetylacetonate ($Fe(acac)_3$) on the surface of ZnO nanorods and its further decomposition to iron oxide nanoparticles

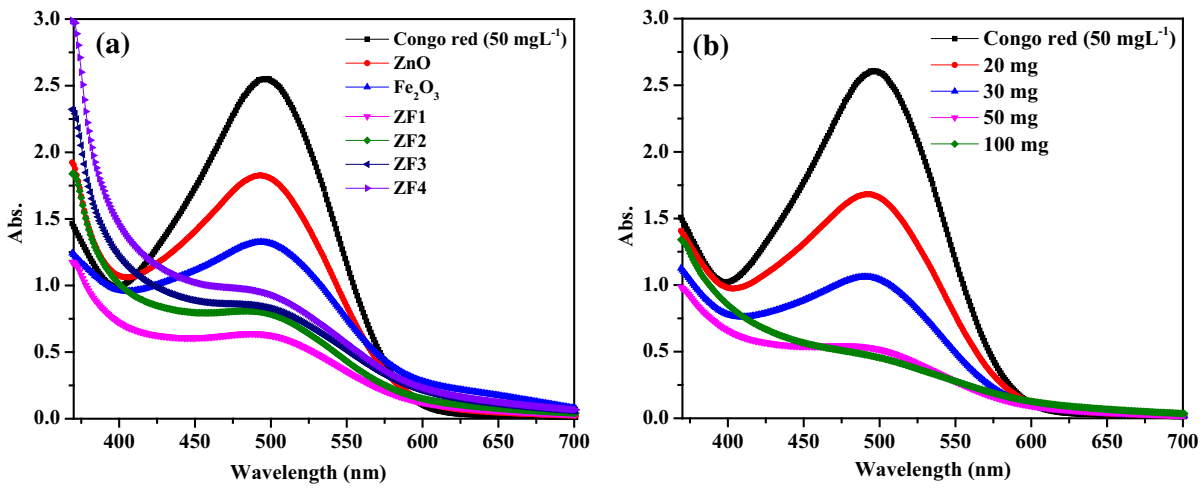

Fig. 11 **a** UV–Visible spectral results on the photocatalytic degradation of congo red in an aqueous solution by ZnO nanorods, γ-Fe_2O_3 nanoparticles and ZnO@γ- Fe_2O_3 core–shell nanocomposites (ZF1, ZF2, ZF3 and ZF4) and **b** UV–Visible spectral results on the photocatalytic degradation of congo red using different amounts of ZnO@γ-Fe_2O_3 core–shell nanocomposite ZF1 as the catalyst

carried out. Congo red ($C_{32}H_{22}N_6O_6S_2Na_2$) is an anionic azo dye used widely in printing, textile, and photographic industries (Liu et al. 2015a, b). The residual congo red in water can cause serious environmental hazard and health problems (Abdullah Mirzaie et al. 2012). Hence, it is necessary to remove congo red from waste water by an efficient and low-cost process. Due to its complex aromatic structure, congo red is stable and it is hard to remove it by traditional methods of waste water treatment. The UV–Visible absorption spectrum of congo red is characterized by a band at 495 nm due to the azo chromophore which leads to its dark red colour. The other two bands at 237 and 343 nm are attributed to benzene and naphthalene rings, respectively (Wang et al. 2008). Figure 11a shows the UV–Visible

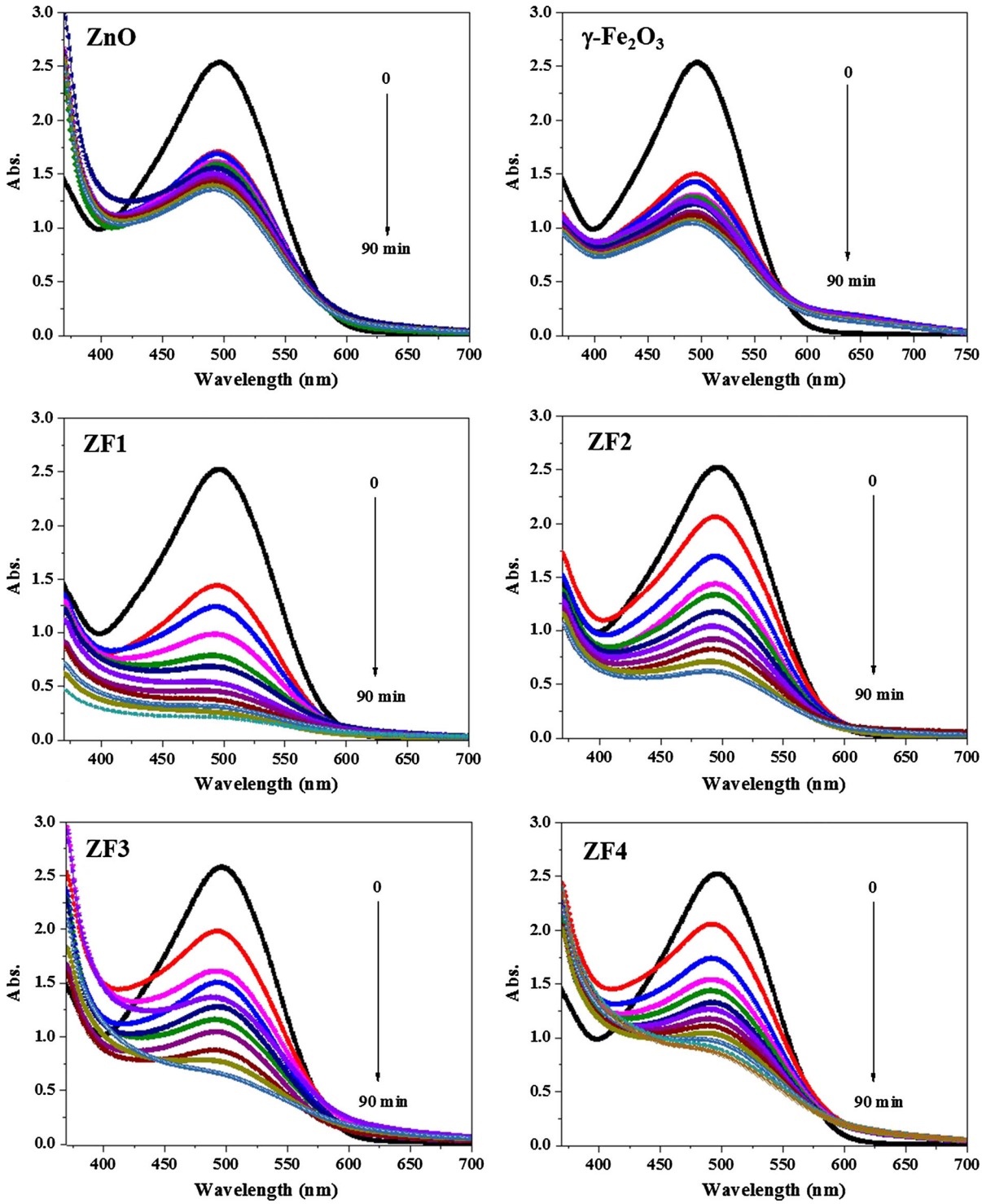

Fig. 12 Kinetics of photodegradation of congo red in aqueous solutions as indicated by UV–Visible spectroscopy using pure ZnO nanorods, γ-Fe_2O_3 nanoparticles and ZnO@γ-Fe_2O_3 core–shell nanocomposites ZF1, ZF2, ZF3 and ZF4 as the catalyst

spectral results on the photodegradation of congo red using pure ZnO nanorods, γ-Fe_2O_3 nanoparticles (before calcination) and all the nanocomposites (ZF1–ZF4) as the catalyst. It can be seen that ZnO@γ-Fe_2O_3 nanocomposite ZF1 shows maximum photodegradation compared to pure ZnO nanorods, γ-Fe_2O_3 nanoparticles and all the other three nanocomposites (ZF2, ZF3 and ZF4). Figure 11b shows the effect of varying the amount of nanocomposite ZF1 on the photocatalytic degradation of congo red. The amount of catalyst was varied from 20 to 100 mg in 50 mL of congo red solution (50 mg L^{-1}). 50 and 100 mg of the catalyst show almost the same extent of decrease in the concentration of congo red and hence, 50 mg of catalyst (ZF1) in 50 mL of congo red solution was optimized as the best condition to carry out further photocatalytic degradation experiments.

Figure 12 shows the kinetics of photocatalytic degradation of congo red by ZnO, γ-Fe_2O_3 nanoparticles and the ZnO@γ-Fe_2O_3 core–shell nanocomposites (ZF1, ZF2, ZF3 and ZF4). In the case of ZnO@γ-Fe_2O_3 core–shell nanocomposite ZF1, the intensity of absorption band of congo red at 495 nm decreases with time and almost becomes zero in about 90 min. On the other hand, pure ZnO, γ-Fe_2O_3 nanoparticles and the other ZnO@γ-Fe_2O_3 nanocomposites (ZF2, ZF3 and ZF4) are unable to complete the degradation during this period. Figure 13a shows comparison of kinetic results on photodegradation of congo red using ZnO, γ-Fe_2O_3 nanoparticles and the ZnO@γ-Fe_2O_3 core–shell nanocomposites as the catalyst where C_o is the initial concentration of congo red and C is its concentration at different times. Nanocomposite ZF1 shows better activity than that of pure ZnO nanorods, γ-Fe_2O_3 nanoparticles and all the other (ZF2, ZF3 and ZF4) nanocomposites. This is because it exhibits effective charge separation, more surface area (The BET surface area values for ZF1, ZF2, ZF3 and ZF4, ZnO and γ-Fe_2O_3 are 62.1, 53.3, 50.3, 38.2, 24.4, and 51.1 m^2/g, respectively) and more number of oxygen vacancies are present on its surface. As elucidated by PL studies in Fig. 8, nanocomposite ZF1 has enhanced defect emission compared to pure ZnO nanorods, γ-Fe_2O_3 nanoparticles and all the other ZnO@γ-Fe_2O_3 nanocomposites (ZF2, ZF3 and ZF4). The photocatalytic activity of metal oxides increases with an increase in the amount oxygen vacancies. The defects and vacancies act as electron acceptors and trap the photogenerated electrons to reduce the surface recombination of electrons and holes (Wang et al. 2009).

The photocatalytic activity of ZnO@γ-Fe_2O_3 core–shell nanocomposites decreases with an increase in the concentration of $Fe(acac)_3$ used during the synthesis of the nanocomposites. The ZnO@γ-Fe_2O_3 core–shell nanocomposite with less amount of γ-Fe_2O_3 nanoparticles (ZF1) shows enhanced photocatalytic activity. It is proposed that presence of higher γ-Fe_2O_3 content (e.g. ZF2, ZF3, and ZF4) causes reduction in the

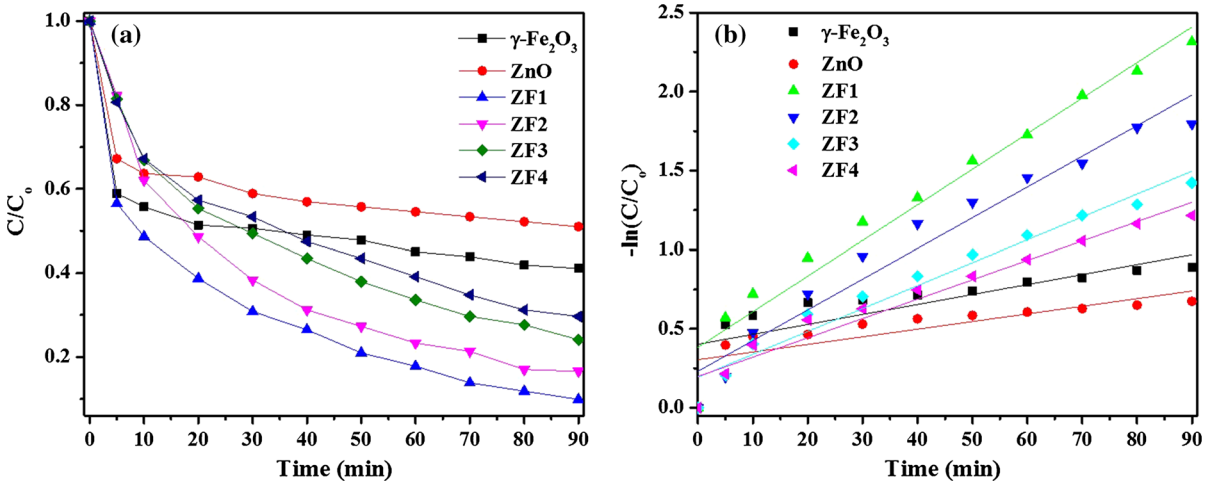

Fig. 13 **a** Comparison of kinetics of photocatalytic degradation of congo red using ZnO nanorods, γ-Fe_2O_3 nanoparticles and ZnO@γ-Fe_2O_3 core–shell nanocomposites (ZF1–ZF4) as the catalyst (C_o is the initial concentration and C is the concentration of dye at different times), and **b** pseudo-first-order kinetics plots for congo red photodegradation. *Symbols* are experimental values and *solid lines* are the fits obtained using pseudo first-order kinetic model

distance between photoelectrons and holes, which results in decrease in the photocatalytic activity due to enhancement in the recombination (Abdullah Mirzaie et al. 2012; Hernández et al. 2007). ZnO@γ-Fe_2O_3 core–shell nanocomposites with lower concentration of $Fe(acac)_3$ (0.15 and 0.1 M) were prepared and their photocatalytic activity was tested and compared with that of nanocomposite ZF1 (prepared using 0.25 M of $Fe(acac)_3$). It was found that nanocomposite ZF1 possesses better activity than the nanocomposites prepared using lower concentrations of $Fe(acac)_3$ (0.15 M and 0.1 M). It is proposed that when the amount of γ-Fe_2O_3 in the nanocomposites is too low, an efficient interfacial electron transfer from γ-Fe_2O_3 to ZnO does not occur. Nanocomposite ZF1 contains an optimum amount of γ-Fe_2O_3 and exhibits maximum degradation efficiency due to the sensitization of ZnO with γ-Fe_2O_3 with effective visible-light absorption and charge separation at the interface.

In general, the photodegradation of congo red catalyzed by the semiconductors follows pseudo-first-order rate law (Wu et al. 2012).

$$\ln\left[\frac{C_o}{C}\right] = k_1 t$$

where C_o and C represent the concentration of congo red at $t = 0$ and at any time t and k_1 is the apparent first-order rate constant. Figure 13b shows the fitting of kinetics data using pseudo-first-order rate law for the photodegradation of congo red using ZnO nanorods, γ-Fe_2O_3 nanoparticles and ZnO@γ-Fe_2O_3 core–shell nanocomposites (ZF1–ZF4) as the catalysts. The kinetic parameters obtained using the pseudo-first-order kinetic model are summarized in Table 5. The pseudo-first-order rate constant of congo red degradation using ZnO@γ-Fe_2O_3 core–shell nanocomposite ZF1 is 0.022 min^{-1} which is higher than the values for pure ZnO (0.005 min^{-1}), pure γ-Fe_2O_3 (0.006 min^{-1}) and other ZnO@γ-Fe_2O_3 core–shell nanocomposites (ZF2 (0.019 min^{-1}), ZF3 (0.014 min^{-1}) and ZF4 (0.012 min^{-1}). The enhanced activity of ZnO@γ-Fe_2O_3 core–shell nanocomposites compared to ZnO and γ-Fe_2O_3 is attributed to faster charge separation at the interface of ZnO@γ-Fe_2O_3 core–shell nanocomposites.

Table 5 Estimated pseudo-first-order kinetic parameters for the photocatalytic degradation of congo red using pure ZnO, γ-Fe_2O_3 nanoparticles and ZnO@γ-Fe_2O_3 core–shell nanocomposites as the catalysts

Catalyst	Rate constant (min^{-1})	R^2
γ-Fe_2O_3	0.006	0.80
ZnO	0.005	0.78
ZF1	0.022	0.98
ZF2	0.019	0.98
ZF3	0.014	0.97
ZF4	0.012	0.97

The ability of reusing the ZnO@γ-Fe_2O_3 nanocomposite ZF1 was evaluated by performing repeated photocatalytic degradation experiments using congo red solution (50 mg L^{-1}). The suspension containing the catalyst was first irradiated in sunlight for 90 min. The photocatalyst was recovered from the suspension after every cycle by centrifugation and subsequent washing with double distilled water for three times. The recovered catalyst was dried in vacuum for overnight and was reused for the photodegradation. The degradation efficiency of the ZnO@γ-Fe_2O_3 core–shell nanocomposite ZF1 decreases from about 97 to 85 % after four cycles. Magnetic parameters are important for the nanocomposites since they will lead to development of nanocatalysts which are magnetic too. In liquid phase reactions, magnetic separation is an useful approach for removing and recycling catalysts by applying an external magnetic field (Xuan et al. 2009; Ye et al. 2010). A photograph showing magnetic separation of nanocomposite ZF1 (which is superparamagnetic) by applying an external magnetic field from an aqueous suspension, is shown in Fig. S7. The mechanism of photodegradation of congo red by ZnO@γ-Fe_2O_3 nanocomposites is discussed below.

ZnO has absorption in the UV region due to its wide band gap (3.28 eV) and γ-Fe_2O_3 has absorption in the visible region due to its narrow band gap (1.9–2.2 eV) (Yin et al. 2014). The absorption spectra of ZnO@γ-Fe_2O_3 core–shell nanocomposites have contribution from both the components. All the core–shell nanocomposites (ZF1–ZF4) show better photocatalytic efficiency compared to pure ZnO nanorods and γ-Fe_2O_3 nanoparticles. The detailed positions of energy bands for ZnO and γ-Fe_2O_3 are shown in Scheme 2 (Hsu et al. 2015; Kaneti et al. 2014; Pradhan et al. 2012; Wu et al. 2012; Zhang et al. 2015). The presence of γ-Fe_2O_3 nanoparticles on the surface of ZnO nanorods leads to formation of a heterojunction barrier at the interface. This is due to the difference in their work functions (5.0 eV for ZnO and 5.88 eV for

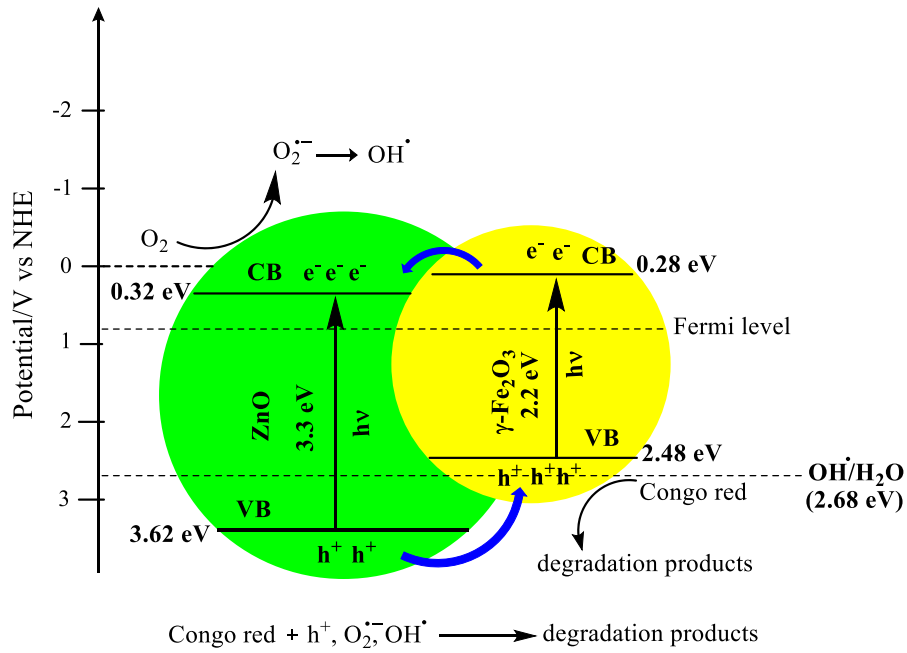

Scheme 2 Schematic diagram of band configuration and electron–hole separation at the interface between ZnO nanorods and γ-Fe_2O_3 nanoparticles under sunlight irradiation

γ-Fe_2O_3) (Kaneti et al. 2014). Since the work function of γ-Fe_2O_3 is higher than that of ZnO, the Fermi level of γ-Fe_2O_3 is lower than that of ZnO. Transfer of electrons occurs from the conduction band of γ-Fe_2O_3 to that of ZnO to equalize the Fermi energy levels which would make the conduction band of ZnO lower than that of γ-Fe_2O_3 (Hsu et al. 2015; Zhang et al. 2011, 2015). The conduction band and valence band potentials of ZnO shift to 0.32 and 3.62 eV, respectively. On sunlight irradiation, electrons in the valence band (VB) of γ-Fe_2O_3 and ZnO are excited to their conduction bands (CB) and at the same time, equal amount of holes are left in the VB. The photogenerated electrons in the CB of γ-Fe_2O_3 are transferred to that of ZnO, while the photogenerated holes in VB of ZnO are transferred to that of γ-Fe_2O_3. As a result, separation of the photogenerated electrons and holes are achieved at the ZnO@γ-Fe_2O_3 interface. This would reduce recombination of electrons and holes and enable them to move to the surface of γ-Fe_2O_3 and ZnO, respectively. The electrons on the surface of ZnO react with dissolved O_2 to give super oxide radical anions ($O_2^{\bullet-}$). The superoxide radicals hydrolyze to form hydroperoxyl radicals ($HO_2^{\bullet}$) which undergo subsequent hydrolysis to form $OH^{\bullet}$ radicals (Wu et al. 2012). The photogenerated holes in the VB of γ-Fe_2O_3 cannot produce $OH^{\bullet}$ radicals by oxidizing H_2O since the VB potential of γ-Fe_2O_3 (+2.48 eV vs. NHE) is higher than $E(OH^{\bullet}/H_2O)$ (+2.68 eV vs. NHE) (Kumar et al. 2013). The photogenerated holes directly oxidize the congo red (Chen et al. 2010b; Konstantinou and Albanis 2004). The photocatalytic mechanism is summarized as follows.

$$ZnO@\gamma\text{-}Fe_2O_3 + h\nu \rightarrow (ZnO)e^- + (\gamma - Fe_2O_3)h^+$$

$$(ZnO)e^- + O_2 \rightarrow O_2^{\bullet-}$$

$$O_2^{\bullet-} + H_2O \rightarrow HO_2^{\bullet} + HO^-$$

$$HO_2^{\bullet} + H_2O \rightarrow H_2O_2 + OH^{\bullet}$$

$$H_2O_2 \rightarrow 2OH^{\bullet}$$

$$\text{Congo red} + h^+, O_2^{\bullet-}, OH^{\bullet} \rightarrow \text{degradation products}$$

To verify the role of various oxidizing species (h^+, $OH^{\bullet}$ and $O_2^{\bullet-}$) in the photocatalytic degradation of congo red, different scavengers were added to the congo red solution before addition of the catalyst (nanocomposite ZF1). The scavengers used were ammonium oxalate (AO), benzoquinone (BQ), and tertiary butyl alcohol (t-BuOH) as h^+, $O_2^{\bullet-}$ and $OH^{\bullet}$ scavengers, respectively (Wang et al. 2011; Yang et al.

2016; Zhiyong et al. 2015). About 0.07 g of solid AO, 0.09 g of BQ, and 0.48 mL of t-BuOH were added to 50 mL of congo red aqueous solution (50 mg L^{-1}) to make a scavenger concentration of 10 mM in each case. The photodegradation results after the introduction of scavengers are shown in Fig. S8. It can be seen from Fig. S8, when AO (holes scavenger) was added to the suspension, the congo red degradation is considerably suppressed as compared to that in the absence of AO, confirming h^+ as active species in the degradation. On the addition of BQ ($O_2^{\cdot-}$ scavenger), the congo red degradation is again suppressed to a significant extent. However, the addition of t-BuOH ($OH^{\cdot}$ scavenger) does not affect the degradation much. On the basis of the above results, it is proposed that h^+ and $O_2^{\cdot-}$ play important role in the photocatalytic degradation of congo red in an aqueous solution over ZnO@γ-Fe_2O_3 core–shell nanocomposites as the catalyst in the presence of sunlight.

Recently, many authors have reported photodegradation of congo red in the presence of different nanocomposites. Abdullah Mirzaie et al. have reported photodegradation of congo red in the presence of ZnO–Fe_2O_3 nanocomposites (Abdullah Mirzaie et al. 2012). The nanocomposite having (Fe^{3+}/Zn^{2+}) molar ratio of 1/100 shows the highest photocatalytic activity of about 93 % decolorization in 25 min compared to other nanocomposites (Fe^{3+}/Zn^{2+} = 0.5/100, 5/100 and 10/100). Narayan et al. have reported photocatalytic degradation of congo red (25 mg L^{-1}) in the presence of Y^{3+} doped TiO_2 nanocomposites. They observed maximum rate constant of 0.027 min^{-1} for nanocomposite $TiO_2(Y_2O_3)_{0.1}$ with 91 % of degradation in about 180 min (Narayan et al. 2009). Pouretedal and Keshavarz have reported photodegradation of congo red (5 mg L^{-1}) in the presence of $Zn_{1-x}Cu_xS$ nanocomposites. They observed rate constant of 0.033 min^{-1} for nanocomposite $Zn_{0.9}Cu_{0.1}S$ with 98 % degradation in about 120 min (Pouretedal and Keshavarz 2010). Jiang et al. have reported photodegradation of congo red (20 mg L^{-1}) in the presence of γ-Fe_2O_3-CdS nanocomposite. They observed rate constant of 0.0023 min^{-1} with 91.5 % of degradation in about 300 min (Jiang et al. 2014). Guo et al. have reported photodegradation of congo red (50 mg L^{-1}) in the presence of TiO_2-PANI nanocomposites. They observed maximum rate constant of 0.0007 min^{-1} for nanocomposite (1:1) with 95 % photodegradation in about 160 min (Guo et al. 2014). Farbod et al. have reported photodegradation of congo red (20 mg L^{-1}) in the presence of Gd-TiO_2 nanocomposites. They observed rate constant of 0.034 min^{-1} for the nanocomposite Gd(1.8 %)-TiO_2 with complete photodegradation in about 180 min (Farbod and Kajbafvala 2013). Lin et al. have reported photodegradation of congo red in the presence of ZnO-Zn nanocomposite with cellulose (ZnO/Zn)–C and starch (ZnO/Zn)–S. They observed rate constant of 0.0105 min^{-1} for (ZnO/Zn)–S with 98 % of photodegradation in about 3 h (Lin et al. 2014). Thiripuranthagan et al. have reported photodegradation of congo red (50 mg L^{-1}) in the presence of Ag impregnated TiO_2–SiO_2 composites. They observed rate constant of 0.0173 min^{-1} for TiO_2–SiO_2 impregnated with 1 % Ag with 85 % of photodegradation in about 180 min (Thiripuranthagan et al. 2015). Liu et al. have reported photodegradation of congo red (25 mg L^{-1}) in the presence of Ag-ZnO nanocomposites. They observed a rate constant of 0.0312 min^{-1} for 3 % Ag-ZnO nanocomposite with 97.3 % of photodegradation in about 50 min (Liu et al. 2015). Li et al. have reported photodegradation of congo red (10 mg L^{-1}) in the presence of TiO_2/PCNFs (porous carbon nanofibers). They observed a rate constant of 0.0158 min^{-1} for nanocomposite TiO_2/PCNFs-4 (0.25 mL of $TiCl_4$) for complete photodegradation in about 60 min (Li et al. 2015). In the present work, complete photodegradation of congo red takes place in about 90 min with a rate constant of 0.022 min^{-1} by the ZnO@γ-Fe_2O_3 nanocomposite ZF1.

Conclusions

ZnO@γ-Fe_2O_3 core–shell nanocomposites were synthesized by a novel thermal decomposition approach. The nanocomposites were characterized with various instrumental techniques. XRD results confirm the presence of wurtzite ZnO and studies on as-prepared and calcined samples suggest the phase of as-prepared iron oxide nanoparticles as γ-Fe_2O_3. FT-IR results on ZnO@γ-Fe_2O_3 core–shell nanocomposites show characteristic IR bands due to γ-Fe_2O_3 and FE-SEM images show formation of uniform iron oxide shell on the ZnO nanorods. Transmission electron microscopy studies on the ZnO@γ-Fe_2O_3 core–shell nanocomposites show uniform shell (10 nm-20 nm) of γ-Fe_2O_3

nanoparticles coated on the ZnO nanorods. HRTEM observations demonstrate that the constituents of the nanocomposites are crystalline with characteristics lattice spacing due to γ-Fe_2O_3 (0.48 nm) and ZnO (0.24 nm). Diffuse reflectance spectra of ZnO@γ-Fe_2O_3 core–shell nanocomposites indicate extended optical absorption in the visible range of 400–600 nm. The core–shell nanocomposites show red shift of band gap absorption due to iron oxide from 2.24 to 1.9 eV with an increase in the precursor concentration of γ-Fe_2O_3. The photoluminescence spectral studies indicate that the ZnO@γ-Fe_2O_3 nanocomposites exhibit enhanced defect emission and the ZnO@γ-Fe_2O_3 core–shell nanocomposites exhibit superparamagnetic behaviour at room temperature with maximum saturation magnetization of 2.1 emu/g. The ZnO@γ-Fe_2O_3 core–shell nanocomposites show better photocatalytic efficiency towards degradation of congo red in aqueous solutions compared to ZnO nanorods and γ-Fe_2O_3 nanoparticles. The enhancement in activity is attributed to stronger visible-light absorption and effective charge separation at the interface of ZnO@γ-Fe_2O_3 core–shell nanocomposites.

Acknowledgments P. J thanks the Council of Scientific and Industrial Research (CSIR), New Delhi for the financial support (Project No. 01(2726)/13/EMR-II). The award of Research Fellowship to Mr. Sudheer Kumar Yadav by the University Grants Commission, Government of India, is gratefully acknowledged. The authors are also thankful to the Institute Instrumentation Centre, Indian Institute of Technology Roorkee for providing the facilities.

References

Abdullah Mirzaie R, Kamrani F, Anaraki Firooz A, Khodadadi AA (2012) Effect of α-Fe_2O_3 addition on the morphological, optical and decolorization properties of ZnO nanostructures. Mater Chem Phys 133:311–316. doi:10.1016/j.matchemphys.2012.01.029

Amin N, Arajs S (1987) Morin temperature of annealed submicronic α-Fe_2O_3 particles. Phys Rev B 35(10):4810–4811. doi:10.1017/CBO9781107415324.004

Apte SK, Naik SD, Sonawane RS, Kale BB, Baeg JO (2007) Synthesis of nanosize-necked structure α- and γ-Fe_2O_3 and its photocatalytic activity. J Am Ceram Soc 90(2):412–414. doi:10.1111/j.1551-2916.2006.01424.x

Ayyappan S, Gnanaprakash G, Panneerselvam G, Antony MP, Philip J (2008) Effect of surfactant monolayer on reduction of Fe_3O_4 nanoparticles under vacuum. J Phys Chem C 112(47):18376–18383. doi:10.1021/jp8052899

Azizi K, Heydari A (2014) Vitamin B1 supported on silica-encapsulated γ-Fe_2O_3 nanoparticles: design, characterization and application as a greener biocatalyst for highly efficient acylation. RSC Adv 4(17):8812–8816. doi:10.1039/c3ra46437g

Balti I, Smiri LS, Rabu P, Gautron E, Viana B, Jouini N (2014) Synthesis and characterization of rod-like ZnO decorated with γ-Fe_2O_3 nanoparticles monolayer. J Alloys Compd 586:S476–S482. doi:10.1016/j.jallcom.2013.02.118

Bødker F, Hansen MF, Koch CB, Lefmann K, Mørup S (2000) Magnetic properties of hematite nanoparticles. Phys Rev B 61(10):6826–6838. doi:10.1103/PhysRevB.61.6826

Chandraiahgari CR, De Bellis G, Ballirano P, Balijepalli SK, Kaciulis S, Caneve L, Sarto F, Sarto MS (2015) Synthesis and characterization of ZnO nanorods with a narrow size distribution. RSC Adv 5(62):49861–49870. doi:10.1039/C5RA02631H

Chen D, Xu R (1998) Hydrothermal synthesis and characterization of nanocrystalline γ-Fe_2O_3 particles. J Solid State Chem 137(9):185–190. doi:10.1006/jssc.1997.7631

Chen C, Ma W, Zhao J (2010a) Semiconductor-mediated photodegradation of pollutants under visible-light irradiation. Chem Soc Rev 39(11):4206–4219. doi:10.1039/b921692h

Chen YJ, Zhang F, Zhao GG, Fang XY, Jin HB, Gao P, Zhu CL, Cao MS, Xiao G (2010b) Synthesis, multi-nonlinear dielectric resonance, and excellent electromagnetic absorption characteristics of Fe_3O_4/ZnO core/shell nanorods. J Phys Chem C 114(20):9239–9244. doi:10.1021/jp912178q

Chu XY, Hong X, Zhang XT, Zou P, Liu YC (2008) Heterostructures of ZnO microrods coated with iron oxide nanoparticles. J Phys Chem C 112(41):15980–15984. doi:10.1021/jp804590y

Farbod M, Kajbafvala M (2013) Effect of nanoparticle surface modification on the adsorption-enhanced photocatalysis of Gd/TiO_2 nanocomposite. Powder Technol 239:434–440. doi:10.1016/j.powtec.2013.02.027

Fu R, Wang W, Han R, Chen K (2008) Preparation and characterization of γ-Fe_2O_3/ZnO composite particles. Mater Lett 62(25):4066–4068. doi:10.1016/j.matlet.2008.05.006

Guo N, Liang Y, Lan S, Liu L, Zhang J, Ji G, Gan S (2014) Microscale hierarchical three-dimensional flowerlike TiO_2/PANI composite: synthesis, characterization, and its remarkable photocatalytic activity on organic dyes under UV-light and sunlight irradiation. J Phys Chem C 118(32):18343–18355. doi:10.1021/jp5044927

Guskos N, Glenis S, Zolnierkiewicz G, Typek J, Sibera D, Kaszewski J, Moszyński D, Łojkowski W, Narkiewicz U (2010) Magnetic study of Fe_2O_3/ZnO nanocomposites. Phys B Condens Matter 405(18):4054–4058. doi:10.1016/j.physb.2010.06.055

Hernández A, Maya L, Sánchez-Mora E, Sánchez EM (2007) Sol–gel synthesis, characterization and photocatalytic activity of mixed oxide ZnO-Fe_2O_3. J Sol-Gel Sci Technol 42(1):71–78. doi:10.1007/s10971-006-1521-7

Hsu YK, Chen YC, Lin YG (2015) Novel ZnO/Fe_2O_3 core–shell nanowires for photoelectrochemical water splitting. ACS Appl Mater Interfaces 7(25):14157–14162. doi:10.1021/acsami.5b03921

Jayanthi SA, Nathan DMGT, Jayashainy J, Sagayaraj P (2015) A novel hydrothermal approach for synthesizing α-Fe_2O_3, γ-Fe_2O_3 and Fe_3O_4 mesoporous magnetic nanoparticles. Mater Chem Phys 162:316–325. doi:10.1016/j.matchemphys.2015.05.073

Jiang R, Yao J, Zhu H, Fu Y, Guan Y, Xiao L, Zeng G (2014) Effective decolorization of congo red in aqueous solution by adsorption and photocatalysis using novel magnetic alginate/γ-Fe_2O_3/CdS nanocomposite. Desalin Water Treat 52(1–3):238–247. doi:10.1080/19443994.2013.787551

Kaneti YV, Zakaria QMD, Zhang Z, Chen C, Yue J, Liu M, Jiang X, Yu A (2014) Solvothermal synthesis of ZnO-decorated α-Fe_2O_3 nanorods with highly enhanced gas-sensing performance toward n-butanol. J Mater Chem A 2:13283–13292. doi:10.1039/C4TA01837K

Kishore PNR, Jeevanadam P (2011) Synthesis of silver–iron oxide nanocomposites by thermal decomposition. J Nanosci Nanotechnol 11(4):3445–3453. doi:10.1166/jnn.2011.3748

Kishore PNR, Jeevanandam P (2012) A novel thermal decomposition approach for the synthesis of silica-iron oxide core-shell nanoparticles. J. Alloys Compd 522(1):51–62. doi:10.1016/j.jallcom.2012.01.076

Konstantinou IK, Albanis TA (2004) TiO_2-assisted photocatalytic degradation of azo dyes in aqueous solution: kinetic and mechanistic investigations: a review. Appl Catal B Environ 49(1):1–14. doi:10.1016/j.apcatb.2003.11.010

Kumar SG, Rao KSRK (2015) Zinc oxide based photocatalysis: tailoring surface-bulk structure and related interfacial charge carrier dynamics for better environmental applications. RSC Adv 5(5):3306–3351. doi:10.1039/C4RA13299H

Kumar S, Surendar T, Baruah A, Shanker V (2013) Synthesis of a novel and stable g-C_3N_4–Ag_3PO_4 hybrid nanocomposite photocatalyst and study of the photocatalytic activity under visible light irradiation. J. Mater. Chem. A 1(17):5333–5340. doi:10.1039/c3ta00186e

Laurent S, Forge D, Port M, Roch A, Robic C, Elst LV, Muller RN (2008) Magnetic iron oxide nanoparticles: synthesis, stabilization, vectorization, physicochemical characterizations, and biological applications. Chem Rev 108(6):2064–2110. doi:10.1021/Cr068445e

Lee YJ, Jun KW, Park JY, Potdar HS, Chikate RC (2008) A simple chemical route for the synthesis of γ-Fe_2O_3 nanoparticles dispersed in organic solvents via an iron–hydroxy oleate precursor. J Ind Eng Chem 14(1):38–44. doi:10.1016/j.jiec.2007.08.009

Li X, Lin H, Chen X, Niu H, Zhang T, Liu J, Qu F (2015) Fabrication of TiO_2/porous carbon nanofibers with superior visible photocatalytic activity. New J Chem 39(10):7863–7872. doi:10.1039/C5NJ01189B

Lin CR, Chu YM, Wang SC (2006) Magnetic properties of magnetite nanoparticles prepared by mechanochemical reaction. Mater Lett 60(4):447–450. doi:10.1016/j.matlet.2005.09.009

Lin ST, Thirumavalavan M, Jiang TY, Lee JF (2014) Synthesis of ZnO/Zn nano photocatalyst using modified polysaccharides for photodegradation of dyes. Carbohydr Polym 105(1):1–9. doi:10.1016/j.carbpol.2014.01.017

Liu S, Ma C (2015) Synthesis and characterization of flower-like NiCoP/ZnO composites. New J Chem 39(8):6332–6337. doi:10.1039/C5NJ00992H

Liu Y, Yu L, Hu Y, Guo C, Zhang F, Lou XW (2012) A magnetically separable photocatalyst based on nest-like γ-Fe_2O_3/ZnO double-shelled hollow structures with enhanced photocatalytic activity. Nanoscale 4(1):183–187. doi:10.1039/c1nr11114k

Liu X, Li W, Chen N, Xing X, Dong C, Wang Y (2015a) Ag–ZnO heterostructure nanoparticles with plasmon-enhanced catalytic degradation for Congo red under visible light. RSC Adv 5(43):34456–34465. doi:10.1039/C5RA03143E

Liu Y, Sun L, Wu J, Fang T, Cai R, Wei A (2015b) Preparation and photocatalytic activity of ZnO/Fe_2O_3 nanotube composites. Mater Sci Eng B 194:9–13. doi:10.1016/j.mseb.2014.12.021

Ma J, Wang K, Zhan M (2015) Growth mechanism and electrical and magnetic properties of Ag–Fe_3O_4 core–shell nanowires. ACS Appl Mater Interfaces 7(29):16027–16039. doi:10.1021/acsami.5b04342

Maiti D, Mukhopadhyay S, Chandra Mohanta S, Saha A, Sujatha Devi P (2015) A multifunctional nanocomposite of magnetic γ-Fe_2O_3 and mesoporous fluorescent ZnO. J Alloys Compd 653(1):187–194. doi:10.1016/j.jallcom.2015.08.230

Maity D, Agrawal DC (2007) Synthesis of iron oxide nanoparticles under oxidizing environment and their stabilization in aqueous and non-aqueous media. J Magn Magn Mater 308(1):46–55. doi:10.1016/j.jmmm.2006.05.001

Mashlan M, Zboril R, Machala L, Vujtek M, Walla J, Nomura K (2004) Mössbauer spectroscopy in study of thermally induced crystallization of amorphous Fe_2O_3 nanoparticles. J Metastab Nanocryst Mater 20–21:641–647. doi:10.4028/www.scientific.net/JMNM.20-21.641

Maya-Treviño ML, Guzmán-Mar JL, Hinojosa-Reyes L, Ramos-Delgado NA, Maldonado MI, Hernández-Ramírez A (2014) Activity of the ZnO-Fe_2O_3 catalyst on the degradation of Dicamba and 2,4-D herbicides using simulated solar light. Ceram Int 40(6):8701–8708. doi:10.1016/j.ceramint.2014.01.088

Mikhaylova M, Kim DK, Bobrysheva N, Osmolowsky M, Semenov V, Tsakalakos T, Muhammed M (2004) Superparamagnetism of magnetite nanoparticles: dependence on surface modification. Langmuir 20(6):2472–2477. doi:10.1021/la035648e

Mo M, Ma T, Jia L, Peng L, Guo X, Ding W (2009) Ferric oxide and $ZnFe_2O_4$ nanotubes derived from nano ZnO/FeO_x core/shell structures. Mater Lett 63(26):2233–2235. doi:10.1016/j.matlet.2009.07.041

Morales MP, Veintemilas-Verdangure S, Montero MI, Serna CJ, Roig A, Casas L, Martinez B, Sandiumenge F (1999) Surface and internal spin canting in γ-Fe_2O_3 nanoparticles. Chem Mater 11(12):3058–3064. doi:10.1021/cm991018f

Mukherjee S, Pal AK, Bhattacharya S, Chattopadhyay S (2008) Field-induced spin–flop transitions of interacting nanosized α-Fe_2O_3 particles dispersed in a silica glass matrix. J Phys Condens Matter 20(5):055204/1–055204/12. doi:10.1088/0953-8984/20/05/055204

Nadeem K, Krenn H, Traussnig T, Würschum R, Szabó DV, Letofsky-Papst I (2011) Effect of dipolar and exchange interactions on magnetic blocking of maghemite nanoparticles. J Magn Magn Mater 323(15):1998–2004. doi:10.1016/j.jmmm.2011.02.041

Narayan H, Alemu H, Macheli L, Thakurdesai M, Rao TKG (2009) Synthesis and characterization of Y^{3+}-doped TiO_2 nanocomposites for photocatalytic applications.

Nanotechnology 20(25):255601/1–255601/8. doi:10.1088/0957-4484/20/25/255601

Pandey BK, Shahi AK, Shah J, Kotnala RK, Gopal R (2014) Optical and magnetic properties of Fe_2O_3 nanoparticles synthesized by laser ablation/fragmentation technique in different liquid media. Appl Surf Sci 289:462–471. doi:10.1016/j.apsusc.2013.11.009

Phu ND, Ngo DT, Hoang LH, Luong NH, Chau N, Hai NH (2011) Crystallization process and magnetic properties of amorphous iron oxide nanoparticles. J Phys D Appl Phys 44(34):345002/1–345002/7. doi:10.1088/0022-3727/44/34/345002

Pouretedal HR, Keshavarz MH (2010) Synthesis and characterization of $Zn_{1-x}Cu_xS$ and $Zn_{1-x}Ni_xS$ nanoparticles and their applications as photocatalyst in congo red degradation. J Alloys Compd 501(1):130–135. doi:10.1016/j.jallcom.2010.04.058

Pradhan GK, Martha S, Parida KM (2012) Synthesis of multifunctional nanostructured zinc-iron mixed oxide photocatalyst by a simple solution-combustion technique. ACS Appl Mater Interfaces 4(2):707–713. doi:10.1021/am201326b

Qin L, Zhu Q, Li G, Liu F, Pan Q (2012) Controlled fabrication of flower–like ZnO–Fe_2O_3 nanostructured films with excellent lithium storage properties through a partly sacrificed template method. J Mater Chem 22(15):7544–7550. doi:10.1039/c2jm30277b

Ramachandra TV, Jain R, Krishnadas G (2011) Hotspots of solar potential in India. Renew Sustain Energy Rev 15(6):3178–3186. doi:10.1016/j.rser.2011.04.007

Reda SM (2010) Synthesis of ZnO and Fe_2O_3 nanoparticles by sol–gel method and their application in dye-sensitized solar cells. Mater Sci Semicond Process 13(5–6):417–425. doi:10.1016/j.mssp.2011.09.007

Saffari J, Mir N, Ghanbari D, Khandan-Barani K, Hassanabadi A, Hosseini-Tabatabaei MR (2015) Sonochemical synthesis of Fe_3O_4/ZnO magnetic nanocomposites and their application in photo-catalytic degradation of various organic dyes. J Mater Sci Mater Electron 26(12):9591–9599. doi:10.1007/s10854-015-3622-y

Schimanke G, Martin M (2000) In situ XRD study of the phase transition of nanocrystalline maghemite (γ-Fe_2O_3) to hematite (α-Fe_2O_3). Solid State Ionics 136–137(1):1235–1240. doi:10.1016/S0167-2738(00)00593-2

Si S, Li C, Wang X, Yu D, Peng Q, Li Y (2005) Magnetic monodisperse Fe_3O_4 nanoparticles. Cryst Growth Des 5(2):391–393. doi:10.1021/cg0497905

Si S, Li C, Wang X, Peng Q, Li Y (2006) Fe_2O_3/ZnO core-shell nanorods for gas sensors. Sensors Actuators B Chem 119(1):52–56. doi:10.1016/j.snb.2005.11.050

Song YB, Song XD, Cheng CJ, Zhao ZG (2015) Poly(4-styrenesulfonic acid-co-maleic acid)-sodium-modified magnetic reduced graphene oxide for enhanced adsorption performance toward cationic dyes. RSC Adv 5(106):87030–87042. doi:10.1039/C5RA18255G

Sreeja V, Joy PA (2007) Microwave-hydrothermal synthesis of γ-Fe_2O_3 nanoparticles and their magnetic properties. Mater Res Bull 42(8):1570–1576. doi:10.1016/j.materresbull.2006.11.014

Suresh R, Giribabu K, Manigandan R, Stephen A, Narayanan V (2014) Fabrication of Ni–Fe_2O_3 magnetic nanorods and application to the detection of uric acid. RSC Adv 4(33):17146–17155. doi:10.1039/c4ra00725e

Teja AS, Koh PY (2009) Synthesis, properties, and applications of magnetic iron oxide nanoparticles. Prog Cryst Growth Charact Mater 55(1–2):22–45. doi:10.1016/j.pcrysgrow.2008.08.003

Thiripuranthagan S, Raj D, Kannan K (2015) Photocatalytic degradation of congo red on silica supported Ag impregnated TiO_2. J Nanosci Nanotechnol 15(6):4727–4733. doi:10.1166/jnn.2015.9795

Tsuzuki T, Schäffel F, Muroi M, McCormick PG (2011) Magnetic properties of mechanochemically synthesized γ-Fe_2O_3 nanoparticles. J Alloys Compd 509(17):5420–5425. doi:10.1016/j.jallcom.2011.02.073

Wang J, Li R, Zhang Z, Sun W, Xu R, Xie Y, Xing Z, Zhang X (2008) Efficient photocatalytic degradation of organic dyes over titanium dioxide coating upconversion luminescence agent under visible and sunlight irradiation. Appl Catal A Gen 334(1–2):227–233. doi:10.1016/j.apcata.2007.10.009

Wang J, Liu P, Fu X, Li Z, Han W, Wang X (2009) Relationship between oxygen defects and the photocatalytic property of ZnO nanocrystals in nafion membranes. Langmuir 25(2):1218–1223. doi:10.1021/la803370z

Wang Y, Deng K, Zhang L (2011) Visible light photocatalysis of BiOI and its photocatalytic activity enhancement by in situ ionic liquid modification. J Phys Chem C 115(29):14300–14308. doi:10.1021/jp2042069

Wang Y, Wang Q, Zhan X, Wang F, Safdar M, He J (2013) Visible light driven type II heterostructures and their enhanced photocatalysis properties: a review. Nanoscale 5(18):8326–8339. doi:10.1039/c3nr01577g

Wilson JL, Poddar P, Frey NA, Srikanth H, Mohomed K, Harmon JP, Kotha S, Wachsmuth J (2004) Synthesis and magnetic properties of polymer nanocomposites with embedded iron nanoparticles. J Appl Phys 95(3):1439–1443. doi:10.1063/1.1637705

Woo K, Hong J, Choi S, Lee H, Ahn J, Kim CS, Lee SW (2004) Easy synthesis and magnetic properties of iron oxide nanoparticles. Chem Mater 16(14):2814–2818. doi:10.1021/cm049552x

Wu H, Wang L (2014) Phase transformation-induced crystal plane effect of iron oxide micropine dendrites on gaseous toluene photocatalytic oxidation. Appl Surf Sci 288(1):398–404. doi:10.1016/j.apsusc.2013.10.046

Wu P, Du N, Zhang H, Jin L, Yang D (2010) Functionalization of ZnO nanorods with γ-Fe_2O_3 nanoparticles: layer-by-layer synthesis, optical and magnetic properties. Mater Chem Phys 124(2–3):908–911. doi:10.1016/j.matchemphys.2010.08.009

Wu W, Zhang S, Xiao X, Zhou J, Ren F, Sun L, Jiang C (2012) Controllable synthesis, magnetic properties, and enhanced photocatalytic activity of spindlelike mesoporous α-Fe_2O_3/ZnO core-shell heterostructures. ACS Appl Mater Interfaces 4(7):3602–3609. doi:10.1021/am300669a

Wu W, Jiang C, Roy VAL (2015) Recent progress in magnetic iron oxide–semiconductor composite nanomaterials as promising photocatalysts. Nanoscale 7(1):38–58. doi:10.1039/c4nr04244a

Xuan S, Jiang W, Gong X, Hu Y, Chen Z (2009) Magnetically separable Fe_3O_4/TiO_2 hollow spheres: fabrication and photocatalytic activity. J Phys Chem C 113(2):553–558. doi:10.1021/jp8073859

Yang G, Zhang B, Wang J, Xie S, Li X (2015) Preparation of polylysine-modified superparamagnetic iron oxide nanoparticles. J Magn Magn Mater 374:205–208. doi:10.1016/j.jmmm.2014.08.040

Yang X, Qian F, Zou G, Li M, Lu J, Li Y, Bao M (2016) Facile fabrication of acidified g-C_3N_4/g-C_3N_4 hybrids with enhanced photocatalysis performance under visible light irradiation. Appl Catal B Environ 193:22–35. doi:10.1016/j.apcatb.2016.03.060

Ye M, Zhang Q, Hu Y, Ge J, Lu Z, He L, Chen Z, Yin Y (2010) Magnetically recoverable core-shell nanocomposites with enhanced photocatalytic activity. Chem: Eur J 16(21):6243–6250. doi:10.1002/chem.200903516

Yin Q, Qiao R, Zhu L, Li Z, Li M, Wu W (2014) α-Fe_2O_3 decorated ZnO nanorod-assembled hollow microspheres: synthesis and enhanced visible-light photocatalysis. Mater Lett 135:135–138. doi:10.1016/j.matlet.2014.07.149

Yu L, Peng X, Ni F, Li J, Wang D, Luan Z (2013) Arsenite removal from aqueous solutions by γ-Fe_2O_3-TiO_2 magnetic nanoparticles through simultaneous photocatalytic oxidation and adsorption. J Hazard Mater 246–247:10–17. doi:10.1016/j.jhazmat.2012.12.007

Zhang L, Papaefthymiou GC, Ying JY (1997) Size quantization and interfacial effects on a novel γ-Fe_2O_3/SiO_2 magnetic nanocomposite via sol–gel matrix-mediated synthesis. J Appl Phys 81(10):6892/1–6892/10. doi:10.1063/1.365233

Zhang J, Liu X, Wang L, Yang T, Guo X, Wu S, Wang S, Zhang S (2011) Synthesis and gas sensing properties of α-Fe_2O_3@ZnO core-shell nanospindles. Nanotechnology 22(18):185501/1–185501/7. doi:10.1088/0957-4484/22/18/185501

Zhang S, Ren F, Wu W, Zhou J, Xiao X, Sun L, Liu Y, Jiang C (2013) Controllable synthesis of recyclable core-shell γ-Fe_2O_3@SnO_2 hollow nanoparticles with enhanced photocatalytic and gas sensing properties. Phys Chem Chem Phys 15(21):8228–8236. doi:10.1039/c3cp50925g

Zhang R, Wang L, Deng J, Zhou T, Lou Z, Zhang T (2015) Hierarchical structure with heterogeneous phase as high performance sensing materials for trimethylamine gas detecting. Sensors Actuators B Chem 220(1):1224–1231. doi:10.1016/j.snb.2015.07.036

Zhiyong Y, Ruiying Q, Huanrong L, Zhiyin W, Xiaohong M, Chaonan D (2015) Preparation and photocatalytic activity of SnO_2. Mater Lett 170(1):25–30. doi:10.1016/j.matlet.2015.12.100

Zhou X, Xiao Y, Wang M, Sun P, Liu F, Liang X, Li X, Lu G (2015) Highly enhanced sensing properties for ZnO nanoparticle-decorated round-edged α-Fe_2O_3 hexahedrons. ACS Appl Mater Interfaces 7(16):8743–8749. doi:10.1021/acsami.5b01071

Zysler RD, Fiorani D, Testa AM (2001) Investigation of magnetic properties of interacting Fe_2O_3 nanoparticles. J Magn Magn Mater 224(1):5–11. doi:10.1016/S0304-8853(00)01328-7